B. C. Tappan, S. A. Steiner III, and E. P. Luther

DOI: 10.1002/anie.200902994

Porous Materials

Nanoporous Metal Foams

Bryce C. Tappan, Stephen A. Steiner III,* and Erik P. Luther*

Keywords:
aerogels · metals · nanofoams · nanostructures · porous materials

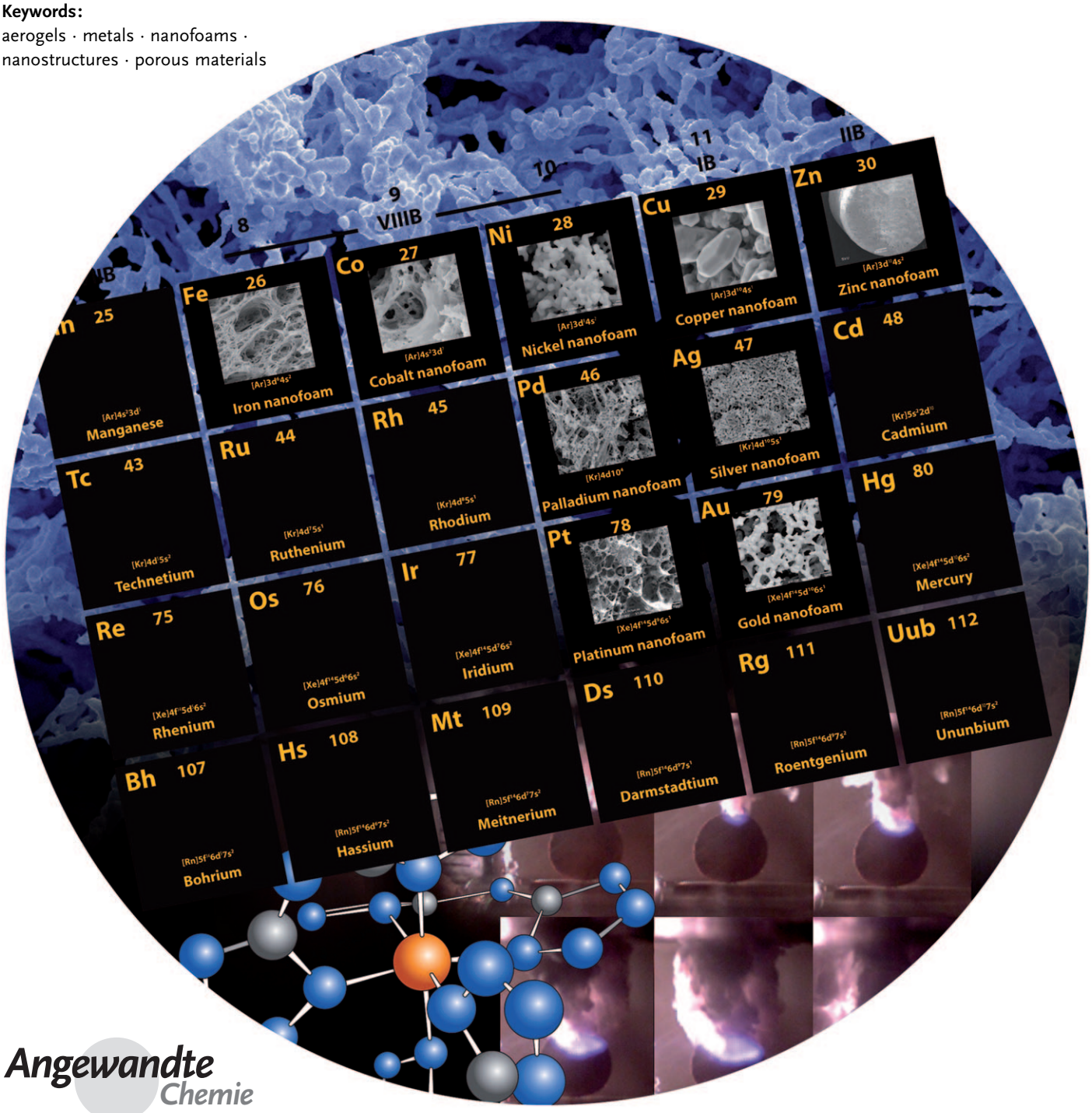

Angewandte International Edition Chemie

Nanoporous metal foams (NMFs) have been a long sought-after class of materials in the quest for high-surface-area conductive and catalytic materials. Herein we present an overview of newly developed synthetic strategies for producing NMFs along with an in-depth discussion of combustion synthesis as a versatile and scalable approach for the preparation of nanoporous, nanostructured metal foams. Current applications of NMFs prepared using combustion synthesis are also presented including hydrogen storage and catalysis.

From the Contents

1. Introduction

For many applications, nanoporous metal foams (NMFs) represent the ultimate form factor of a metal. NMFs combine properties characteristic of metals, such as good electrical and thermal conductivity, catalytic activity, and ductility/malleability with the extreme materials properties characteristic of nanoarchitectures, such as aerogels, which include high surface area, ultralow density, and high strength-to-weight ratio. Additionally, nanostructuring metals results in size-effect enhancements in properties such as catalytic activity[1–5] and plasmonic resonance,[6] further distinguishing the potential of NMFs over bulk forms of metals.

Synthetic strategies for preparing nanoporous foams of many nonmetallic substances exist, including foams (aerogels) of silica;[7–9] main group, transition, lanthanide, and actinide metal oxides;[10–16] metal chalcogenides;[17,18] metal phosphides;[19] carbon;[20,21] organic polymers;[20,22] and even carbon nanotubes.[23,24] Additionally, numerous approaches for preparing macrocellular foams of various metals exist,[25,26] such as foaming of metal alloys using bubbled gas or decomposition of metal hydrides,[27,28] investment casting,[25,29] chemical vapor deposition onto polymer foam templates,[30] and cooling of liquid metal/hydrogen solutions through their eutectic points (the GASAR process).[25,26,31,32] There are also several well-established approaches for preparing thin films of nanoporous metals, most notably through dealloying[33–35] but also recently through deposition of metals onto nanostructured templates[36,37] and laser etching.[38] Turning metals into three-dimensional nanoporous foams, however, has posed itself to be a significant challenge, and only recently have viable synthetic strategies for doing so emerged. Currently, four major approaches for preparing NMFs or closely related materials have been demonstrated: templating,[39] sol–gel assembly of prefabricated nanoparticles,[18] nanosmelting of hybrid polymer–metal oxide aerogels,[40,41] and combustion synthesis.[42]

In this Review, we assess the scope and potential of these four approaches and present an in-depth discussion of combustion synthesis employing metal bistetrazolamine (MBTA) complexes as a versatile platform for preparing nanostructured, nanoporous metal foams of a large number of metals and alloys.

2. The Technological Potential of NMFs

We define a nanoporous metal foam as a three-dimensional structure comprised of interconnected metallic particles or filaments which exhibits a porosity of no less than 50% and in which sub-micron pores (including micropores, mesopores, and macropores 50–1000 nm in diameter) measurably contribute to the specific surface area of the foam.

Indeed, NMFs straddle previously unoccupied parameter space in the plot of pore size versus relative density for porous, low-density metallic materials (Figure 1). Metals having these characteristics take on several interesting materials properties as a consequence, for example, low relative density (ρ_{foam}/ρ_{bulk}), high specific surface area, enhanced plasmonic behavior, and size-effect-enhanced catalytic behavior. NMFs with these characteristics could find utility in a large number of applications and invite an array of new technological possibilities as well, for example:

Battery-like supercapacitors: High-surface-area, porous metals could be made to out-perform, in terms of conductivity,[43,44] the ultraporous carbon electrodes used in today's supercapacitors (ultracapacitors). They could be tailored for better wetting by electrolytes thereby increasing the double-layer capacitance at the electrode surface. This situation translates to higher energy densities. Additionally, high-surface-area metals allow coupling with other electrochemical effects at the electrode surface, for example, faradaic pseudocapacitance and battery-like chemistry.[45]

[*] Dr. B. C. Tappan, Dr. E. P. Luther
Dynamic and Energetic Materials and Materials Science Divisions,
Los Alamos National Laboratory
Los Alamos, NM 87545 (USA)
Fax: (+1) 505-667-0500
E-mail: btappan@lanl.gov
S. A. Steiner III
Department of Aeronautics and Astronautics
Massachusetts Institute of Technology
Cambridge, MA 02139 (USA)
Fax: (+1) 801-650-1463
E-mail: ssteiner@alum.mit.edu

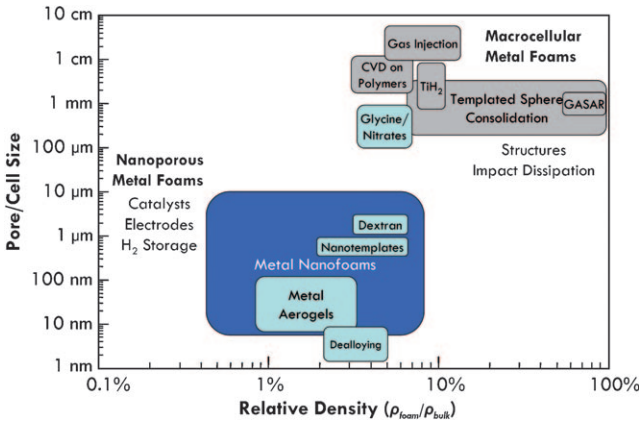

Figure 1. Metal nanofoams occupy new territory in the parameter space of low-density, porous metallic materials.

High power-density batteries: Extending electrode geometries from 2D to 3D has been shown to significantly increase areal power capacity.[45,46] NMFs or derivatives of NMFs could be used to produce enhanced electrodes for batteries, for example, high-surface-area porous zinc for zinc–air batteries. Additionally, the thin struts and open porous "highways" of NMFs provide an ideal environment for rapid mass transport of ions into and out of electrodes and, in turn, faster discharging and recharging batteries.[47]

Viable hydrogen storage: Nanostructured metals have been shown to improve reaction kinetics, lower the uptake and release temperatures, and reduce the enthalpy of formation of metal hydrides.[48] Nanoporous, nanostructured palladium, magnesium, nickel, and lanthanum alloys could thus provide useful scaffoldings for rapid hydrogen uptake and release. Coupled with templated micron-sized channels ("lightning holes") to facilitate rapid mass transport, the nanometer-dimension struts of NMFs could safely and efficiently store and release hydrogen fuel on the time scale required for practical hydrogen vehicles. Furthermore, unlike many other nanomaterial approaches to metal hydride storage, hydridable metal NMFs would also have the ability to efficiently transport heat to and away from sites of hydride formation and decomposition—a major technical hurdle in optimizing reaction kinetics, cyclability, and desorption temperature.[48,49]

Substitutes for platinum-group metals: Size-effect-enhanced catalytic properties of metals such as Au and even common metals such as Ni, suggest that nanostructured foams of these metals could be used to produce catalytic converters competitive with platinum-group metals, which are in diminishing supply, both in terms of turnover per square meter of catalyst and turnover per dollar.[5]

Electromagnetic composites: Combining the loss tangent of a metal with the dielectric constant of air, NMFs fall in a region of electromagnetic parameter space unoccupied by any existing material. This unique pairing of properties could be used to make better passive cooling composites,[50] which can reduce the cost and complexity of satellites by eliminating the need for heavy cooling systems in many cases.

Surface-enhanced Raman spectroscopy (SERS): The coupling of high surface area and enhanced surface plasmonic behavior make NMFs of silver and gold promising for SERS.[6,51,52]

Antimicrobial scaffolds: Silver NMFs could be incorporated in biomedical implants to provide a semi-permanent antimicrobial functionality that can double as a scaffold to promote tissue regrowth.

Filtration and desalination: Conductive porous substrates are of great utility as electrodes in desalination and as ion-exchange membranes. Both carbon aerogels and porous silver have shown promise for these applications.[53–55] Provided the pore size of the substrate can be rendered to diameters on the order of the Debye length of ions in the solution, such substrates could be tailored to selectively transport either positive or negative ions simply by adjusting the potential applied to the electrode.[54]

Lightweight structures: The extreme low density of NMFs optimizes the cube-root of the Young's modulus-to-density ratio that would make NMFs useful as foam cores for ultralight sandwich panel structures.[25]

Heat sinks: Coupling the thermal conductivity of metals with ultrahigh surface area, NMFs represent an efficient form factor for maximizing thermal flux—of great potential value in dissipating heat from integrated circuits and heat exchangers.[56]

Ultra-high-field electromagnets: Optimizing $1/\rho C\kappa$ for a material (where ρ is bulk density, C is specific heat, and κ is electrical conductivity) maximizes the attainable field of an electromagnet with prescribed temperature rise and strength.[25] While macrocellular metal foams optimize this value compared to that of bulk metals, NMFs further optimize the value compared to that of macrocellular metal foams.

Magnetic media: Extending the magnetic advantages of thin-film metals volumetrically, nanoporous magnetic metals

Bryce Tappan received his BS in Chemistry from the New Mexico Institute of Mining and Technology in 1997 and his PhD in Analytical Chemistry from the University of Delaware in 2003, where he specialized in the fabrication of energetic nanomaterials and the decomposition chemistry of energetic materials. In 2003 he joined Los Alamos National Laboratory as a post-doctoral fellow where he is currently a Staff Scientist. His research interests include synthesis and characterization of energetic materials and combustion synthesis.

Stephen Steiner is a PhD candidate at the Massachusetts Institute of Technology and a student affiliate of Los Alamos National Laboratory. He received his BS in Chemistry from the University of Wisconsin in 2004 and his SM in Materials Science and Engineering from MIT in 2006. His research interests include pairing of disparate materials properties through nanoengineering, heterogeneous catalysis of nanostructured carbons, and synthesis of exotic porous materials.

could find utility in applications ranging from data storage to flat-panel speaker cones.

3. Synthesis of NMFs

3.1. The Elusiveness of NMFs

Nanoporous metal foams have been late to develop in comparison with nanoporous foams of other substances. First, bottom-up approaches useful in preparing nanoporous foams of non-metallic substances are not well-suited for metals. For example, aerogels of many different substances can be prepared through supercritical drying of gels in which the solid phase of the gel is composed of the desired substance; however, no synthetic pathways for gels with metallic backbones have yet been demonstrated. Second, top-down approaches useful in preparing macrocellular metal foams encounter problems arising from length-scale-dependent phenomena in scaling to nanometer dimensions. For example, open-celled nickel macrocellular foams with pore sizes in the 100–300 μm range can be produced through electrodeposition or chemical vapor deposition (CVD) of nickel tetracarbonyl onto polymer-foam templates followed by oxidative removal of the template,[25,30] however analogous deposition using CVD or ALD (atomic layer deposition) of metals onto silica or carbon aerogels results in the formation of discrete nanoparticles too sparse, or a thin film too weak to stand as a monolithic structure on its own in isolation from the template, as opposed to a continuous, cohesive conformal coating throughout the aerogel interior.[57–59] Other methods used for preparing macrocellular foams, such as investment casting, are limited by practically attainable melt viscosities, thermal conductivities, and, in the case of the GASAR process, control over nucleation of gas bubbles used to foam the metal.[25,32]

3.2. Characterization Techniques

Techniques useful in characterizing other porous nanoarchitectures are also effective for NMFs. Many NMFs also exhibit significant macroporosity and so optical microscopy can be helpful, however SEM and TEM are needed to appreciate the most relevant porosity. Surface techniques, such as X-ray photoelectron spectroscopy (XPS), Auger spectroscopy, and energy-dispersive X-ray spectroscopy (EDAX) are valuable for characterizing the chemical composition of NMFs and, in the case of XPS, the chemical state of elements at the foam surface. NMFs can also easily be characterized by powder X-ray diffraction (XRD) which, when used in conjunction with surface techniques, can help create a complete compositional profile of the foam. Small-angle scattering techniques utilizing neutrons (SANS) or X-rays (SAXS) are even more powerful analysis tools which enable unambiguous measurement of particle aggregate geometry, particle morphology, particle size distribution, and even specific surface area.[60] Gas sorption isotherms can also be used to calculate specific surface area from Brunauer–Emmett–Teller (BET) theory.[61] Similarly, pore size statistics (for pores ranging from 1.7–300 nm) can be determined from complete adsorption/desorption isotherms using the Barrett–Joyner–Halena (BJH) model.[62] Nitrogen is the preferred analyte for both techniques, however often individual samples of NMFs exhibit relative densities so low ($<1\,\%$) that their total surface area is too small for reliable analysis with nitrogen. In these cases, krypton can be employed instead, although its adsorption behavior only allows for calculation of specific surface area and not pore size statistics. Using both bulk and surface techniques is of critical importance for characterizing NMFs since most procedures for preparing NMFs involve high-temperature processing and, as the resulting materials contain very fine grains and have nanometer-scale features, compositional gradients can become heavily pronounced. This feature translates into compositional variation between the interior of the struts of the foam (important for applications such as hydrogen storage) and the mass-transport-accessible surface porosity (important for catalysis).

We have found surface area per mole as opposed to surface area per unit mass to be a more useful metric for both comparing the surface area of NMFs to other nanoporous materials and gauging catalytic propensity. For example, nanoporous iron monoliths prepared in our laboratory exhibit surface areas as high as 258 $m^2 g^{-1}$, approximately three-times lower than per-mass surface area values typically reported for mesoporous carbon aerogels (ca.750 $m^2 g^{-1}$).[22] Taking into consideration atomic weight, however, the nanoporous iron foam has a molar surface area of 11 400 $m^2 mol^{-1}$ compared with only 9000 $m^2 mol^{-1}$ for the carbon aerogels. In other words, the nanoporous iron foam has a larger surface area per surface-accessible atom. Thus, herein we report specific surface area both by mole and by mass.

Erik Luther earned his BS in Ceramic Engineering from Rutgers University in 1990. He went on to study Materials Science at UCSB and received his PhD from there in 1995. From 1995 to 1997, he joined the Princeton Materials Institute as a post-doctoral fellow. He then worked as part of a start-up R&D company to develop nanosized perovskite materials after which he joined Los Alamos National Laboratory as a Staff Scientist. His research focus is in the area of hydrogen storage.

3.3. Templating and Dealloying Approaches

One seemingly straightforward approach for preparing NMFs is deposition of metals onto a template structure of the desired pore size, for example, arrays of colloidal silica particles (also called colloidal crystals) or polystyrene (latex) spheres. Infiltration into templates with sub-micron features, however, proves to be quite challenging in practice, as the interstitial regions of such arrays are narrow and thus difficult to penetrate/wet by metals or metal precursors. Jiang et al.

have demonstrated an electroless deposition technique successful in penetrating the interstitial spaces of such templates that is extensible to a variety of metals including Ni, Cu, Au, Pt, and Ag.[63] In this approach, Au nanoparticles are deposited onto a template of thiol-functionalized colloidal silica spheres with a diameter of a few hundred nm. The resulting monolayer of gold then allows for facile electroless depositions for a potentially wide variety of metals. The process gives free-standing thin films with ordered, monodisperse pores ranging from 200–600 nm, with reasonably high surface areas of 590–1760 $m^2 mol^{-1}$ in the case of Ni (10–30 $m^2 g^{-1}$). A similar technique demonstrated by Yan et al. using a different deposition process on arrays of ordered, monodisperse polystyrene spheres enables production of films with 250–500 nm pore sizes.[64] In their technique, solution-phase nickel acetoacetonate is infiltrated into the array of spheres. Wetting is facilitated by selection of a suitable solvent, for example, ethanol/water mixture or acetic acid. The acetoacetonate salt is precipitated by a second infiltration of the template with oxalic acid. The salt-coated template is finally calcined or reduced under H_2 to afford NiO or Ni, respectively, and the template is burned away to leave a free-standing porous film that exhibits surface areas comparable to those of Jiang et al. Both templating approaches, while limited to thin films, produce materials with regular, ordered porosity—of critical importance for optical and metamaterial applications.

A variant on templating used in the production of disordered nanoporous metal thin films is dealloying.[33–35,65] In this method, an alloy of a target metal and one or more relatively more reactive metals is prepared such that a sufficient amount of the target metal is present to create a continuous percolating network (in the case of Au typically over 16 vol%). Alloys of silver and gold or copper and gold are commonly used. The alloy is then etched either electrochemically or with acid to selectively remove the less-noble metal(s), leaving behind a nanoporous framework of the remaining metal. While this approach produces thin films with pores under 100 nm, it scales poorly beyond dimensions of 1 mm because of the diffusion-limited processes required and is thereby restricted to thin films and small monoliths. Additionally, because of the constraints on the chemical reactivity, dealloying is only effective for alloys of a handful of metals. One industrially important example of dealloying is the catalyst known as "Raney nickel" used in numerous reactions including the hydrogenation of alkenes and aromatics, such as the hydrogenation of benzene to cyclohexane.[66] Raney nickel is, in fact, a nanoporous form of Ni produced by leaching Al out of Ni–Al alloys using highly concentrated (ca. 5 M) sodium hydroxide. The resulting material is approximately 85 wt% Ni and exhibits a specific surface area of approximately 4100–5870 $m^2 mol^{-1}$ (ca. 70–100 $m^2 g^{-1}$).[67,68]

A technique for preparing macroscopic monoliths of nanoporous gold foams using dealloying has recently been demonstrated through use of a macropore templating technique similar to that developed by Yan et al. to address the diffusion problems associated with dealloying.[39] In this approach, gold (15 atom%) and silver (85 atom%) are deposited over micron-sized polystyrene spheres through electroless deposition. The metal-coated spheres are then cast into a container by pouring a suspension of the spheres onto filter paper. The polystyrene spheres are next pyrolyzed away under inert atmosphere at 400 °C, leaving behind a macroporous gold–silver foam. Finally, the gold–silver foam is dealloyed by etching with incrementally concentrated solutions of nitric acid, resulting in a hierarchically porous gold foam, that is, a macroporous foam with nanoporous gold walls (Figure 2). Optionally the foams may be supercritically dried from CO_2 to insure preservation of microporosity and mesoporosity.[39] The technique allows the production of nanoporous gold foams with dimensions of several centimeters and in virtually any shape that can be filter cast. Additionally, each of the steps involved is relatively straightforward, although the entire process is somewhat lengthy. However, as the technique is an extension of dealloying, it is limited to only and a handful of elements and alloys. Also, like dealloyed thin films of Au, Au foams produced through this process still contain a significant amount of Ag even after etching (up to 4.4 atom% at the surface).[69–71] For catalyst applications, however, this residual Ag may actually be advantageous, for example, it has been shown that the enhancement in catalytic behavior of dealloyed Au in room-temperature oxidation of CO to CO_2 actually occurs at the nanosized Ag inclusions remaining in the Au.[35]

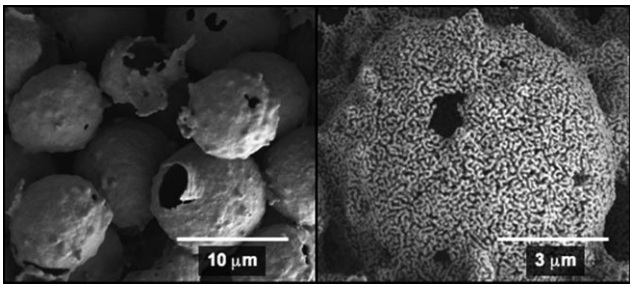

Figure 2. Hierarchically porous Au foam prepared through dealloying of Au–Ag alloys templated onto polystyrene beads (image courtesy Dr. Juergen Biener).

3.4. Sol–Gel Approaches

3.4.1. Direct Assembly of Nanoparticles

Despite the availability of numerous sol–gel techniques for the synthesis of metal and metal-containing nanoparticles, sol–gel pathways that directly assemble metal nanoparticles into gels suitable for supercritical or freeze drying into aerogels have proven to be surprisingly difficult. Brock et al. demonstrate a number of synthetic pathways for producing aerogels of metal chalcogenides and metal phosphides through synthesis of surfactant-stabilized nanoparticles followed by controlled oxidative removal of the surfactant groups to invoke gelation.[18,72,73] Gacoin et al. first explored the viability of preparing gels of metal chalcogenide nanoparticles in depth,[74] the possibility of which was a matter of

debate for some time,[75] and showed that necessary conditions for gelation of metal chalcogenides include 1) a solubility of nanoparticles on the order of about 30 wt% and 2) the ability to controllably remove stabilizing ligands from the nanoparticles to invoke sol–gel assembly. Imparting these lessons to the possibility of making metal aerogels through a similar approach, it stands to reason that metal nanoparticles with high solubility in a polar solvent would be necessary to achieve a sol–gel transition, however the availability of such metal nanoparticles, even from well-developed systems (such as Au), is limited.

To evaluate the potential of this approach for producing metal aerogels, we sought out a formulation of highly water-soluble nanoparticles of a metal with which ligand removal and agglomeration could be attempted. Uzun et al. have demonstrated a technique for producing Au nanoparticles with high water solubility by utilizing a dual-ligand approach[76] that gives Au nanoparticles with solubilities in water of up to 30 wt%. As a proof-of-concept, we oxidized aqueous solutions of these nanoparticles with hydrogen peroxide in concentrations ranging from 2 to 30 wt% using a modified version of the procedure outlined by Gacoin et al. After approximately 48 h following introduction of 30 wt% H_2O_2, porous, nanostructured, orange precipitates resulted (Figure 3). No solid phase appeared with lower concentrations of peroxide. This kind of precipitative sol–gel event, in contrast to a container-wide transition to a gel, highlights one of the challenges underlying development of a direct sol–gel approach for production of nanoporous metal gels and aerogels, in that even approximately 30 wt% of metal nanoparticles such as Au is still too low of a molar concentration to invoke a sol–gel transition. The fact that such agglomerates of nanoparticles form at all, however, suggests that the principle of controlled ligand removal could be used to assemble a gel network of metal nanoparticles that could be subsequently supercritically dried to yield metal aerogels, although high molar solubilities would likely be necessary.

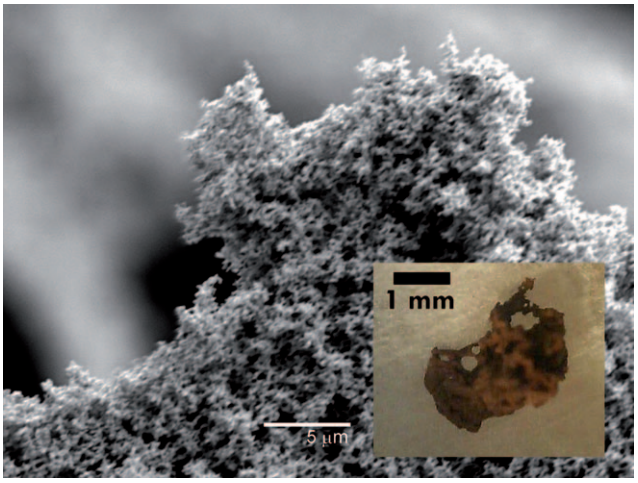

Figure 3. SEM image of the porous structure formed from the precipitation of water-soluble Au nanoparticles by oxidative ligand removal. The formation of this structure indicates how a direct sol–gel approach for the production of Au aerogels might work. Inset: optical microscope image of porous Au precipitate.

3.4.2. Metal Aerogels Derived by Nanosmelting

One of the most effective approaches for producing NMFs to date is the technique demonstrated by Leventis et al., who recently reported the first synthesis of iron aerogels through "nanosmelting" of hybrid polymer/metal oxide aerogels prepared through a sol–gel process.[40,77] The approach is the most direct analogue to the processes used for making other types of aerogels and results in materials that are highly mesoporous (that is, contain a large percentage of pores between 2–50 nm in diameter), exhibit high specific surface areas (ca. 5300 to 16800 $m^2 mol^{-1}$ or ca. 95 to 300 $m^2 g^{-1}$), and have a bulk density 170-times lower than that of bulk iron metal (0.046 $g cm^{-3}$).

The nanosmelting process bears a resemblance to the pyrolytic carbonization technique used for transforming resorcinol–formaldehyde (RF) polymer aerogels into carbon aerogels.[22] The process begins with the formation of a sol–gel-derived hybrid gel comprising interpenetrating nanostructured networks of RF polymer and iron oxide. To produce such a gel, an acid-catalyzed alternative[78] to the RF sol–gel chemistry developed by Pekala[20,22] is combined with the epoxide-assisted gelation of metal salts used for preparing gels of metal oxides developed by Gash and Tillotson,[11] leveraging the Brønsted acidity of metal salts (such as nitrates and chlorides) as both a source for the metal oxide network and a catalyst for RF polymerization.[41] The hybrid RF–iron oxide gel is then supercritically dried to afford a hybrid RF–iron oxide aerogel. Finally, the aerogel is pyrolyzed under Ar at temperatures of 800–1000 °C, during which the RF network dehydrates into carbon (as is the case in synthesis of carbon aerogels) generating CO_2 along with amorphous carbon and CO which concomitantly reduce the iron oxide network to metallic iron. This process is essentially a nanoscale analogue to the smelting of iron oxide with coke used to produce pig iron. While CO is the active reducing agent in the smelting of bulk iron, it is hypothesized that the intimate mixture of nanoparticulate carbon and metal oxide in these materials and comparative lack of oxygen results in direct, solid-state reduction.[79] This solid-state hypothesis is supported by the fact that polymer-cross-linked samples, that is, samples whose skeletal RF/iron oxide networks are conformally coated with polymer (so-called "x-aerogels"), smelt at approximately 400 °C lower than native RF/iron oxide. In these cross-linked samples, the cross-linker melts early (at ca. 200 °C), inducing efficient mixing and reaction of the RF and iron oxide nanoparticles. Depending on the pyrolysis temperature used to smelt the aerogel, the resulting material is a mesoporous foam composed of either a mixture of iron carbides and carbon or nearly pure metallic iron (as shown by powder X-ray diffraction), with only a small portion of residual carbon detectable by EDAX—effectively a "pig iron aerogel" (Figure 4). In total, approximately two-thirds of the mass of the original aerogel is volatilized in this process (Figure 5). Iron aerogels produced through this technique are both magnetic and electrically conductive.

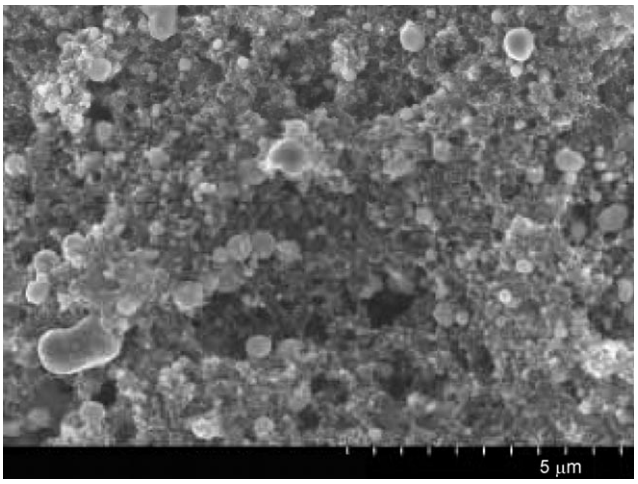

Figure 4. SEM image of iron aerogel derived by nanosmelting of sol–gel-derived hybrid resorcinol–formaldehyde/iron oxide aerogels (image courtesy Dr. Nicholas Leventis).

Figure 5. From left to right: Hybrid resorcinol–formaldehyde/iron oxide aerogel; polyisocyanate cross-linked resorcinol–formaldehyde/iron oxide x-aerogel; mesoporous iron aerogel derived from nanosmelting; macroporous iron aerogel derived from nanosmelting of polyisocyanate-cross-linked x-aerogel (image courtesy Nicholas Leventis).

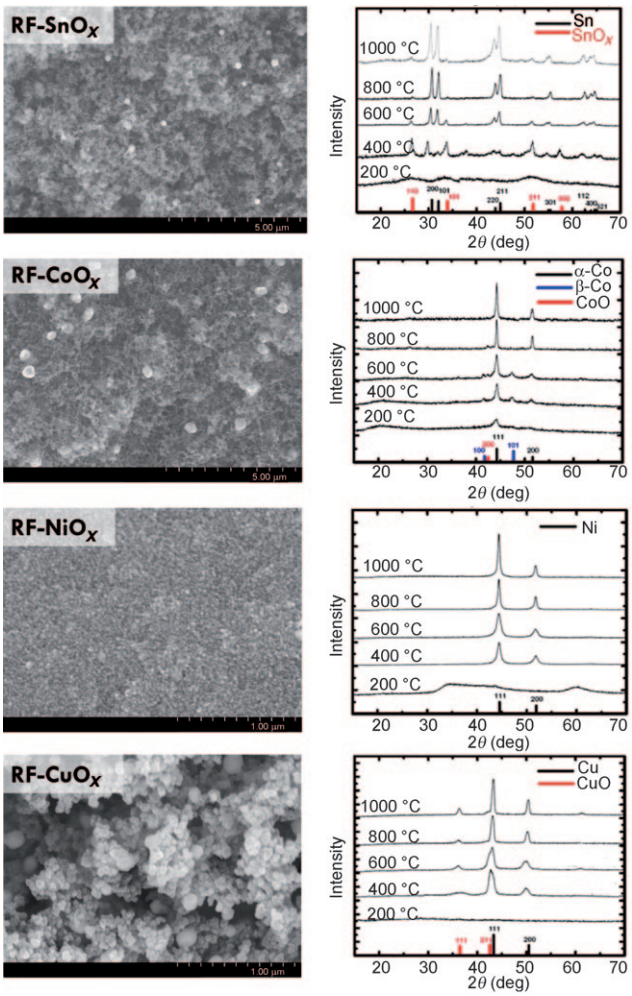

Figure 6. Left: SEM images of hybrid resorcinol–formaldehyde/metal oxide aerogels. Right: temperature-dependence of composition versus smelting temperature of the nanosmelting process as measured by powder XRD[79] (data courtesy Nicholas Leventis).

Nanosmelting has also been demonstrated for Co, Ni, Cu,[80] and the main-group metal Sn (Figure 6). The approach shows tremendous potential as a synthetic pathway for preparing a large variety of nanoporous metal foams and possibly even metal carbide foams. One appealing feature of this process is that both composition and porosity can be tailored through controlled annealing. Additionally, pyrolysis of hybrid resorcinol–formaldehyde/metal oxide x-aerogels cross-linked with polyisocyanates results in macroporous metal foams with pores in the 1–10 micron range—making this approach a valuable method for preparing metal foams with pore sizes that fall between those of NMFs and macrocellular metal foams. Furthermore, the technique utilizes well-established aerogel processing methods and equipment and, in principle, can be scaled to monoliths of any shape and with dimensions in the centimeter range. Like other aerogel materials, however, the technique requires time-consuming diffusion-limited solvent exchanges, and it is unclear if the technique is extensible to metals that do not form stable network oxides (such as Au, for example) or metals such as Ti or Zr that cannot be carbothermically reduced to metal from their oxide.[81–83] In its current stage, monolithicity and shape control are attainable but complicated by change in volume and occasional cracking resulting from pyrolysis; however numerous strategies could potentially be implemented to manage these aspects of the production process.

3.4.3. *Supercritical-Phase Synthesis of Nanostructured Metal Powders*

An early attempt at producing metal aerogels demonstrated a strategy for preparing high-purity, nanostructured powders of metals with aerogel-like characteristics.[84] In this approach, a suspension of a metal acetate in methanol is heated to supercritical conditions, during which the acetate is reduced to a metal by the methanol. The resulting metal atoms subsequently undergo sintering into larger particles which in turn agglomerate. Upon venting of the supercritical methanol, a fine, nanostructured metallic powder remains. While not monolithic, the resulting powders in many ways

resemble the microstructure of monolithic NMFs. Furthermore, the technique is not limited to only smeltable metals and has been demonstrated for Cu, Au, Pd, and alloys of Cu with Pd. The technique is predicted to be extensible to other metals with easily reducible salts, such as Ag, Pt, Bi, Rh, Re, As, Os, Se, and Te, among others.

3.5. Pyrolysis of Metal Salt/Dextran Pastes

Walsh et al. demonstrate a process similar in some respects to nanosmelting in which pastes of the polysaccharide dextran mixed with metal salts are heated between 500–900 °C to afford macroporous metallic sponges of Ag, Au, CuO, and composites thereof.[85] This pyrolytic process results in foams with pores ranging from 1–50 μm in diameter, particles/struts on the order of 1–15 μm, and surface areas on the order of 0.5–1 $m^2 g^{-1}$, depending on temperature and length of heat treatment. Although the foams produced through this technique are not significantly nanoporous or nanostructured, they occupy a useful region of the pore size versus density parameter space between NMFs and macrocellular foams and could potentially serve as interesting precursors to NMFs.

3.6. Combustion Synthesis

Combustion synthesis (also called self-propagating high-temperature synthesis or SHS) refers to techniques that utilize decomposition of energetic substances to produce materials. In these techniques, the inherent energy released from combustion of the precursor mixture drives forward reactions with high activation energy barriers at room temperature. Combustion synthesis techniques exist for a wide range of materials including metal oxides, ceramics, and intermetallics, yielding materials in the form of powdered solids, filaments, and foams.[86]

Recently, Erri et al. produced nickel and nickel/nickel oxide foams with pores ranging from 100 μm–1 mm in diameter through combustion of nickel nitrates with glycine in air.[87] By adjusting the nickel nitrate to fuel ratio, both the composition of the foams and the combustion wave propagation can be controlled. Control over wave propagation is important for enabling formation of foams over powders, which result if the combustion wave propagates too vigorously. In principle the technique is extensible to a wide variety of materials and is significantly less expensive and less toxic than the CVD techniques previously used to prepare Ni foams with comparable pore size to density ratios. However, as the materials produced through this technique are not nanoporous they exhibit relatively low specific surface areas of 50–200 $m^2 mol^{-1}$ (0.8–3.5 $m^2 g^{-1}$).

A different type of combustion synthesis process for preparing NiAl alloy foams has been demonstrated by Hunt et al.[88] In this process, nanometer-sized Al particles are passivated with fluorinated organic ligands ($C_{13}F_{27}COOH$) that double as a gasifying agent. The particles are then mixed with micron-sized Al particles and nanometer-sized Ni particles, pressed into pellets, and laser ignited. The result is the formation of a porous NiAl foam with between 10–80% porosity, depending on the amount of gasifying agent added. These foams could potentially serve as useful precursors to nanoporous Raney Ni foams (which could be prepared by leaching the Al from them with concentrated sodium hydroxide).

Combustion synthesis of metal foams with nanoporous structures was first demonstrated in our laboratory through the use of yet another combustion synthesis technique involving complexes of metals containing the high-nitrogen ligand bis[1(2)H-tetrazol-5-yl]amine (bistetrazolamine or BTA). In this approach, metal bistetrazolamine (MBTA) complexes are synthesized, pressed into pellets, and ignited under inert atmosphere. The result is the formation of metal foams with pores primarily ranging from a few nanometers to several microns in diameter carved out by struts comprised of nanosized particles and filaments (Figure 7). As we will demonstrate in the Section 4, the technique is easily extensible to a wide range of metals and a number of ceramic compositions and affords materials with remarkably high surface areas ranging from 2000–11400 $m^2 mol^{-1}$ (10–260 $m^2 g^{-1}$). We refer to materials produced through combustion synthesis of MBTA complexes as "nanofoams", as they are not only nanoporous but also intrinsically nanostructured—a property that differentiates their potential technological applications markedly from those of macroporous metal foams.

Figure 7. Top left: Fe nanofoam next to an unburnt pellet of FeBTA complex. Top right: Oval- and circle-shaped copper nanofoams. Unlike Fe, Cu nanofoams retain the same shape and size as the unburnt pellet from which they were synthesized. Bottom: Co nanofoams exhibiting porosity ranging from nm to mm.

4. Combustion Synthesis with Metal Bistetrazolamine Complexes

4.1. Origins of the Technique

The technique for producing metal nanofoams using combustion synthesis was discovered during the characterization of a class of energetic salts and transition-metal complexes being developed at Los Alamos. Chavez et al. had synthesized the alkali- and alkaline-earth-metal salts and copper complexes of several members of the tetrazole family (primarily those of bistetrazole (BT) and bistetrazolamine (BTA).[89] Klapötke et al. have since also explored these and other related complexes in depth.[90–104] As energetic additives to pyrotechnics, these compounds produce color through excitation of metal atoms released during combustion, generating primarily only N_2 and CO_2 gas as by-products. This chemistry was later extended to additional transition-metal complexes for which we sought to characterize combustion behavior by determining pressure–dependent burning rates. In attempting to characterize the combustion of the iron BTA (FeBTA) complex, the diagnostic camera observing the interior of the pressure vessel containing a pellet of the compound had become obscured and it was assumed the experiment was a failure. Upon opening the vessel to set up a new experiment, however, an ultralow-density, expanded, gray foam was found, which, on contact with flame, burned in air to yield a rust-colored form of roughly the same dimensions as the original foam. Subsequent characterization of the gray foam revealed a composition of approximately 50 wt% elemental Fe, approximately 50 wt% organic residues, and an intricate, porous nanostructure. Simple reductive heat treatment of the foam under H_2 resulted in what we now call an iron nanofoam.

We have since extended this combustion synthesis process to a wide variety of metals and nonmetals and have explored a number of parameters in efforts to control the morphology and properties of materials produced through this process.

4.2. Phenomenological Description of the Combustion Synthesis Process

4.2.1. Energetic Behavior of High-Nitrogen Complexes

Combustion synthesis of nanofoams is made possible by a somewhat unusual decomposition behavior inherent to complexes of metals containing the BTA ligand. Few energetic nitrogen-containing transition-metal complexes exhibit steady deflagration (a relatively slow, self-sustained combustion event not requiring outside air) during ignition and decomposition and most commonly undergo rapid transit to detonation (a combustion event that occurs at such a fast rate that a supersonic wave is propagated). This is an undesirable outcome for combustion synthesis of monolithic materials, which requires a steady, controlled combustion front that does not blow the precursors apart.

Common examples of energetic metal compounds include the simple salts of metal azides, fulminates, acetylides, picrates, and styfnates, as well as, to name a few, the heavy-metal complexes of 5-*H*-tetrazole, aminonitrotetrazoles, 5-nitrotetrazoles, azotetrazolate, and tetraamine.[105] Many of these materials are not only sensitive to detonation with flame, but often also with slight friction or impact.[106] Table 1 lists the combustion properties of several energetic metal complexes at ambient pressure. (Note: the only simple energetic salts shown are those of hydrazoic acid, as most other simple energetic salts contain oxygen, precluding their utility for combustion synthesis of materials composed of reduced metallic species.) In terms of energetic decomposition, most energetic high-nitrogen metal complexes exhibit an "all-or-nothing" behavior, that is, either extreme sensitivity with tendency to detonate or total lack of any self-sustained energetic decomposition, that is, they are inert. For example, sodium azide has a low heat of formation and does not sustain combustion in the absence of an oxidizer (such as the iron oxide found in the propellant mixtures used to inflate automotive air bags). Transition-metal azides, such as those of copper, silver and lead, however, have very high heats of formation and, upon ignition, with or without confinement, detonate violently, releasing disperse nanoparticles. Even slow, controlled decomposition of silver azide in an electron beam produces disperse, although regular, nanoparticles of silver metal with dimensions on the order of 100 nm.[107]

4.2.2. Metal BTA Complexes and the "Goldilocks" Effect

Table 1 shows the reactivity behavior of complexes prepared with ligands containing bridged tetrazole rings, namely, those of bistetrazole (BT), bistetrazolamine (BTA), and azotetrazole (AzT). Both BT and AzT are similar to BTA, with the exception of an additional nitrogen in the bridge of AzT and the absence of a bridging nitrogen in BT. Despite the structural similarities among the three ligands, the addition or removal of just one nitrogen atom in the bridge of the ligand vastly changes the dynamics of decomposition of derivative metal complexes. Complexes of BT, while sometimes explosive, in most cases are essentially non-combustible, while complexes of AzBT are dangerously sensitive and readily detonate. Complexes of BTA, however, are only mildly energetic. This trend amounts to a "Goldilocks effect"[*] in terms of the utility of complexes for combustion synthesis (Figure 8): complexes of BT self-extinguish in combustion; complexes of AzBT are too energetic to yield monolithic materials; and complexes of BTA are "just right", possessing the balance of energetic behavior and chemical properties required to yield useful materials upon combustion. Thus BTA complexes appear to fall within an exceptional island of combustibility containing the ability to sustain combustion but not detonate, while simultaneously facilitating a reductive environment that enables metallic structures to form. In general, most energetic transition-metal complexes fall on the "too hot" side of the Goldilocks effect, while non-energetic transition metal complexes are "too cold"

[*] "Goldilocks and the Three Bears" is an English language fairytale in which Goldilocks has a series of three-way choices. In each instance she finds one option "just right" and the other two options are opposing extremes ("too hot"/"too cold" etc.).

Table 1: Common high-nitrogen free acids that yield energetic metal salts or energetic metal complexes.

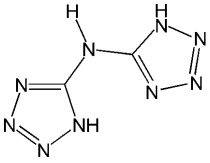	Bistetrazolamine	H^+ Alkali/alkaline earth Transition metals	Fast deflagration Non-combustible Slow deflagration
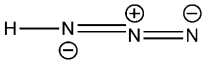	Hydroazoic acid	H^+ Alkali/alkaline earth Transition metals	Detonates Non-combustible Sensitive/detonates
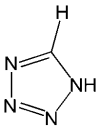	5-H-Tetrazole	H^+ Alkali/alkaline earth Transition metals	Slightly combustible Non-combustible Detonates
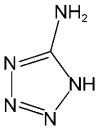	5-Aminotetrazole	H^+ Alkali/alkaline earth Transition metals	Slightly combustible Non-combustible Can detonate
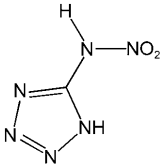	5-Aminonitrotetrazole	H^+ Alkali/alkaline earth Transition metals	Fast deflagration Fast deflagration Sensitive/detonates
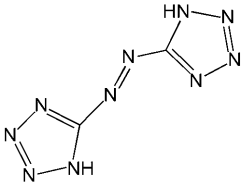	Azotetrazole	H^+ Alkali/alkaline earth Transition metals	Decomposes Very sensitive when dry/detonates Very sensitive/detonates
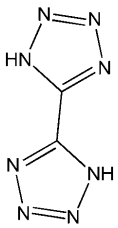	Bistetrazole	H^+ Alkali/alkaline earth Transition metals	Fast deflagration Non-combustible Non-combustible to explosive

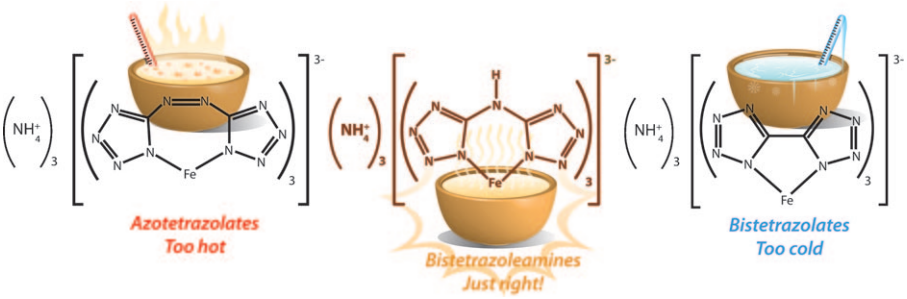

Figure 8. The unique, mild energetic behavior of the bistetrazolamine ligand enables formation of metal nanofoams where similar high-nitrogen ligands are either too inert or too energetic.

4.2.3. *The Transition from Molecules to Foam*

When MBTA complexes undergo the entropy-maximizing process of combustion, the metal atom binding the complex together is reduced to its zero-valent state by nearby nitrogen and carbon centers and is released with significant kinetic energy. These atoms agglomerate into small nanometer-scale grains. These nanoparticulate grains in turn agglomerate together to form larger continuous struts, the assembly of which is guided by expanding N_2 gas, and a nanofoam is "blown". As a consequence, the mean pore size and the mean particle size observed in metal nanofoams are not necessarily correlated. Figure 9 depicts the steps of this process.

Various methods for characterizing the porosity of combustion-synthesized metal nanofoams reveal that the majority of porosity in these materials typically falls between 10 and 200 nm. While pore size statistics from BJH analysis of

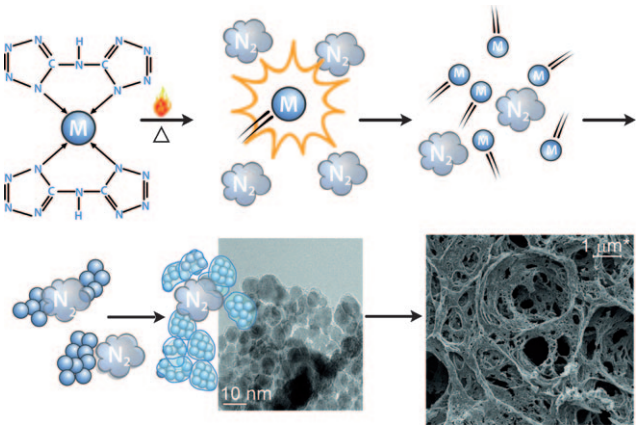

Figure 9. Representation of the dynamic assembly of metal nanofoams by combustion synthesis of metal BTA complexes.

metal nanofoams typically gives values in the mesopore range (2 to 50 nm), a more complete picture is gained when these data are coupled with ultra-small angle neutron scattering (USANS) and SEM image analysis. Figure 10 shows pore size

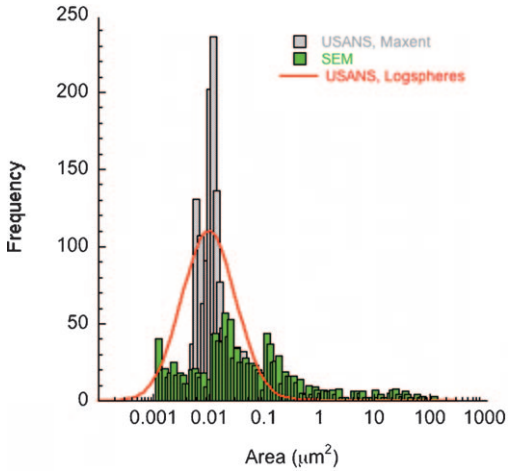

Figure 10. Pore statistics derived from USANS and SEM image analysis for Pt nanofoams, showing pores ranging from 10 to 200 nm in diameter.

distributions derived using both USANS and image analysis for platinum nanofoams formed under an overpressure of 3.6 MPa of Ar. The BJH model for these materials gives pore areas ranging from 1.9–53 000 nm^2, with an average pore area of 9.4 nm^2 (a pore diameter of 3.1 nm). Both USANS and SEM image analysis, however, indicate that the majority of pore areas in these materials falls around 10 000 nm^2 (ca. 100 nm in diameter). Fitting of the USANS data using both a maximum entropy technique ("maxent") and log-normal fit ("logspheres") are found to be in good agreement, as previously observed for small-angle scattering measurements of nanostructured energetic materials.[108] Thus nanofoams can be described as partially mesoporous (pores ranging from 2 to 50 nm), like aerogels, and partially macroporous (pores greater than 50 nm). Since materials exhibiting porosity in the range 50 to 200 nm exhibit markedly higher surface areas than materials with micron-sized pore diameters, also considered macroporous, we find the blanket term "nanoporous" most convenient and appropriate in describing nanofoams, noting that there is no officially agreed upon range of values associated with this term.

While most MBTA complexes that we have surveyed have proven to be only mildly energetic (with the important exception of one BTA complex of gold, see Section 4.5.5), variation in energetic behavior still exists among BTA complexes of the transition metals. Important consequences of this include variation in monolithicity (cohesiveness) and porosity among different nanofoams.

Insight into the assembly mechanism underlying formation of metal nanofoams can be gained by analyzing the heats of formation and calculated adiabatic flame temperatures of different MBTA complexes (see Table 2).[109] Importantly, all of the complexes listed in Table 2 still fall below the melting point of their respective bulk elemental metal. These data suggest that melting does not occur during formation of the foam, but rather that foam assembly occurs by rapid sintering and/or localized surface melting in a highly non-equilibrated state.[110]

We have identified one case in which the adiabatic flame temperature of an MBTA complex appears to be higher than that of the melting point of the nascent metal formed—that of the disilver salt of BTA. High-speed video and post-combustion analysis of this complex make it apparent that higher-than-melting-point flame temperatures are attained. As shown in Figure 11, the combustion of this complex is a highly luminous orange and the resulting silver metal self-sinters into a nonporous ingot. SEM of the product (Figure 11 b,c) confirms that the ingot is indeed heavily sintered, with only a small amount of porosity remaining in certain areas. These results, along with the measurements of the adiabatic flame temperatures of other complexes, indicate that for nanofoam formation to occur, combustion front flame temperatures must remain below the bulk melting point of the metal to inhibit overall sintering of the metal monolith. Thus, based on thermodynamic data for a given MBTA complex, a

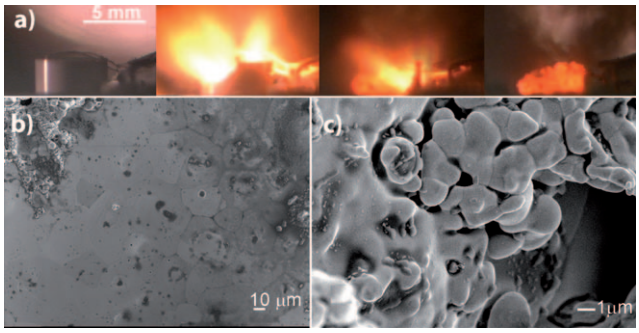

Figure 11. a) Image sequence of Ag_2BTA combustion showing the high-temperature formation and self-sintering of Ag metal, b) SEM image of resulting melt-solidified Ag metal, and c) porous area of resulting Ag metal seen in top left corner of panel (b).

Table 2: Heats of formation and adiabatic flame temperatures of some bistetrazolamine complexes.

Complex name	Chemical formula	Molecular weight	Heat of Formation [kJ mol^{-1}]	Density [g cm^{-3}]	Adiabatic Flame Temperature [K][a]	Melting Point of Bulk Metal/K
Ammonium tris(bis(tetrazolato)amine) Fe^{III}	$C_6H_{15}N_{30}Fe$	563.23	767.8	1.847	1219.3	1811
Ammonium bis(bis(tetrazolato)amine) Ni^{II}	$C_4H_{10}N_{20}Ni$	396.95	−10.4	1.734	621.4	1728
Ammonium tris(bis(tetrazolato)amine) Co^{III}	$C_6H_{15}N_{30}Co$	566.32	781.8	1.856	1237.2	1768
Bis(tetrazolato)amine Cu^{II} diammonia	$C_2H_7N_{11}Cu$	248.70	52.6	1.767	708.0	1358
Ammonium bis(bis(tetrazolato)amine) Pd^{II}	$C_4H_{10}N_{20}Pd$	444.68	336.7	[b]	[b]	1828
Ammonium bis(bis(tetrazolato)amine) Pt^{II}	$C_4H_{10}N_{20}Pt$	533.34	−109.2	[b]	[b]	2041

[a] Calculated at 1.01 bar. [b] Data Unavailable.

rough prediction of the possibility of nanofoam formation by combustion synthesis can be made. Other variables to take into consideration in making this prediction include the ratio of the metal to gas-forming atoms, as well as reduction potential of the metal, that is, whether or not it can be reduced to a zero-valent state with the energy/agents available in the combustion environment.

4.2.4. A Molecularly Integrated Blowing Agent

Another important aspect of the nanofoam assembly involves the role of nitrogen and other gaseous products released during combustion synthesis. A large volume of gas is produced during the decomposition stage of MBTA complexes. This gas effectively serves as an integrated blowing agent, responsible for the formation of the majority of the pores observed in metal nanofoams (ranging from tens to thousands of nanometers). This gas is also important in the reduction of the oxidized metal from the complex to a zero-valent state, and must be relatively free of any oxidizing gas so as to produce a net-reductive (or at least net-oxidation-neutral) environment. Metals that are highly electropositive might be expected to further utilize the nitrogen gas released from the ligand to form metal nitrides. This approach, in fact, has been exploited by Frank et al. to produce disperse nanocrystals of GaN from the detonation synthesis of gallium azides.[111]

4.3. Synthesis of Metal BTA Complexes

One of the advantages of the MBTA combustion synthesis technique lies in the ability to produce a large number of complexes through aqueous chemistry. BTA ligands can be produced by the method described by Naud et al.[112] (see also the syntheses described by Friedrich et al. and Klapötke et al.[90,94]). Briefly, sodium dicyanoamide is treated with sodium azide acidified to a pK_a of less than 1 to produce sodium bistetrazolamine (NaBTA). The NaBTA is then rinsed thoroughly with sodium nitrite ($NaNO_2$) to destroy any residual azides. Next, NaBTA is treated with HCl to produce the free-acid bistetrazolamine monohydrate (BTAw), which is then recrystallized. BTAw is subsequently treated with 2 equivalents of ammonium hydroxide to produce a highly soluble diammonium salt (DA-BTA), which yields a chalky white precipitate of diammonium bistetrazolamine monohydrate (DA-BTAw) upon evaporation.

DA-BTAw can then be treated with any of a number of metal salts, such as chloride, nitrate, or perchlorate salts in aqueous solution to form the desired MBTA complex.[113,114] The crystal structure for CoBTA is shown in Figure 12. The

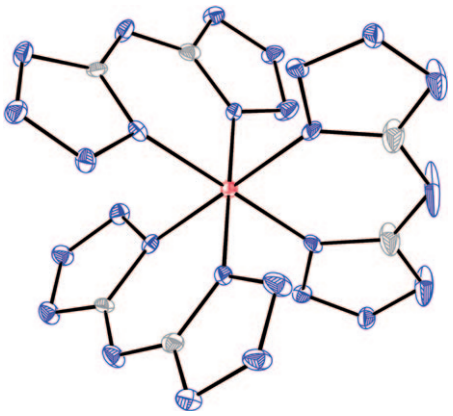

Figure 12. Thermal ellipsoid plot (ellipsoids set at 50% probability) for the crystal structure of the CoBTA complex used for combustion synthesis of Co nanofoams. Gray C, blue N, red Co.

number of BTA ligands that attach to the metal center depends on the chemistry of the metal being used (see Table 3). For example, reaction of DA-BTA with iron perchlorate gives an iron complex with three BTA ligands. Reaction of DA-BTA with auric acid ($HAuCl_4$) gives two complexes, one with two BTA ligands and one water ligand, and another complex with three BTA ligands. In some cases, such as the noble Group 10 metals, low solubility in aqueous solutions limits complex formation and requires heating to proceed efficiently. For example, PdBTA can be synthesized by reaction of ammonium bistetrazolamine ($(NH_4)_2$BTA)

Table 3: Transition-metal bistetrazolamine complexes useful for preparing metal nanofoams by combustion synthesis.

Metal	Number of BTA ligands per metal atom	Monolithicity of nanofoam
Fe	3	Ashy
Co	3	Ashy
Ni	2	Ashy (unassisted combustion) or moderately robust (with Joulean heating of combustion pellet)
Cu	$1 + 2NH_3$	Robust
Ag	0.5	Robust with inclusion of Ag nanoparticles
Au	$2 + 1H_2O$	Robust, elastic
Au	3	Ashy
Pd	2	Ashy (unassisted combustion) or robust (with Joulean heating of combustion pellet)
Pt	2	Ashy (unassisted combustion) or robust (with Joulean heating of combustion pellet)
Ti	2	Robust

with either $K_2[PdCl_4]$ or $[PdCl_2(CH_3CN)_2]$ by mixing a heated solution of $(NH_4)_2$BTA (2 equiv) in water with a heated solution of palladium salt (1 equiv), giving a white or beige precipitate and pale-yellow solution.

Scheme 1 depicts the typical steps involved in the synthesis process from the production of BTA, DA-BTA, and an MBTA complex (in this case FeBTA). A number of MBTA

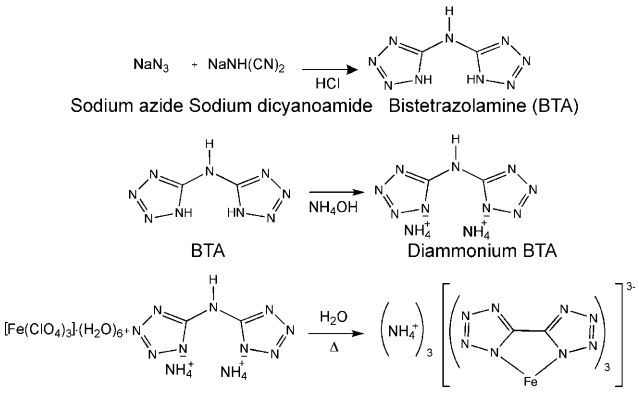

Scheme 1. Reaction scheme for the production of metal BTA complexes.

complexes cannot be prepared through a straightforward aqueous route, such as, those of titanium and perhaps zirconium and hafnium (for example, most Ti starting materials (such as $TiCl_4$) hydrolyze on contact with water). These complexes can instead be prepared through a non-aqueous pathway employing metal alkoxides (see Scheme 2). Instead, TiBTA can be produced by treating titanium isopropoxide ($Ti[OCH(CH_3)_2]_4$) with two equivalents of BTA in anhydrous ethanol. This results in a complex suitable for preparation of Ti nanofoams. Synthesis of Ti nanofoams is described in more detail in Section 4.5.1.

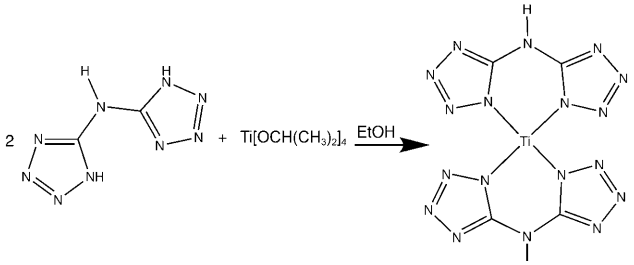

Scheme 2. Non-aqueous synthesis of TiBTA.

4.4. Methods for Controlling Nanofoam Formation

4.4.1. Ignition Method

The primary method we have used for ignition of pressed pellets of MBTA precursors is through a resistively heated nickel–chromium wire. However, laser ignition using a 10.6 μm CO_2 laser is also effective and helpful in both increasing the area of ignition, which makes for a much more reliable and robust combustion, as well as increasing production throughput. Additionally, laser heating is of great utility when ignition of a MBTA precursor is difficult, such as with BTA complexes of the Group 10 metals. These complexes seem to fall at the lower limit of sustainable combustibility and special measures must be undertaken to facilitate a self-propagating combustion front. Laser ignition can also be coupled with the application of an electric current across the combustion-front plasma to assist in ignition across the entire face of a pellet. In other combustion synthesis reactions, this approach has resulted in improvement of materials properties over materials prepared by conventional combustion synthesis techniques, as demonstrated by Munir.[115] Application of electric current is also useful for systems of low reaction enthalpy, low reaction rate, and non-optimum thermal conductivity which cannot form self-sustaining combustion fronts, as is the case with high-density pellets of Group 10 MBTA complexes. For comparison, preheating pellets to 120 °C to drive fully dense Group 10 MBTA complexes to combustion seems to change the combustion wave characteristics and results in excessive grain growth and loss of the finer structure within the nanofoam. Electric current activation is primarily thermal in nature, producing rapid localized Joulean heating during combustion and influencing wave velocity and wave characteristics. Moreover, electric current can induce self-propagation reaction waves in larger precursor density ranges, which can be a determining factor in the size, shape, and distribution of pores in the final product. Better control over wave properties might eventually eliminate the necessity for post-combustion treatments and provide better control over the structural parameters of pores and struts of the foam.

4.4.2. Pressure

Combustion synthesis of metal nanofoams is typically performed in a combustion chamber with an overpressure of inert gas of up to 10.4 MPa. In contrast with most transition-metal energetic materials in which the burning phase quickly

transitions to detonation, MBTA precursors exhibit a pressure-dependent burning rate. An example of this can be seen in FeBTA, which exhibits a factor of five burning rate increase from increasing the over-pressure from 0.1 to 7 MPa.[116] Foam morphology is affected by numerous factors including burning rate and heat transfer; therefore, it comes as no surprise that altering the overpressure affects the foam microstructure. Similarly, changing the inert atmosphere from nitrogen to argon also changes the foam morphology, presumably because of a difference in thermal conductivity between the gases. This pressure effect on nanofoam microstructure is illustrated by SANS measurements of structural components in nanofoams produced from combustion of FeBTA over a range of pressures (Figure 13).

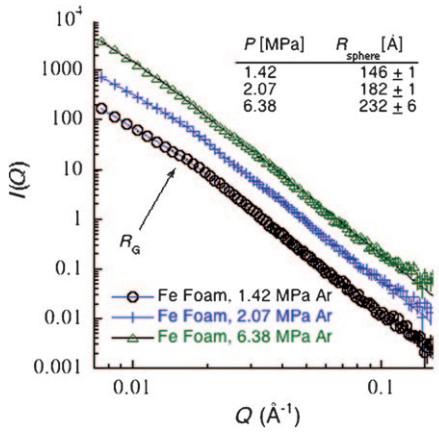

Figure 13. SANS analysis of Fe nanofoams combusted at different over-pressures showing a feature size dependence on the over-pressure. R_{sphere} = sphere radius of foam microstructure, R_G = radius of gyration, $I(Q)$ = scattering intensity, Q = momentum transferred in scattering event.

4.4.3. *Post-Combustion Annealing*

As produced, metal nanofoams from combustion synthesis contain a large percentage of carbon- and nitrogen-containing organic impurities (up to 50 wt%). These impurities can be removed through volatilization under inert atmosphere or by annealing the nanofoam under H_2 at elevated temperatures (ca. 500°C). Interestingly, prior to purification, Fe and Co nanofoams, while predominantly metallic, are not magnetic, whereas the as-produced Ni nanofoam is strongly magnetic. After heat-treatment, all three nanofoams exhibit strong ferromagnetism, this is in part due to purification but mostly due to ordering of nanocrystalline and amorphous phases.

4.4.4. *Inclusion of Gas Generates*

As mentioned in the discussion of adiabatic flame temperatures versus nascent metal melting point in Section 4.2.3, combustion of Ag_2BTA results in a primarily densified silver product as opposed to a silver nanofoam. While portions of this product may take on some characteristics of a typical nanofoam, the majority of the ingot is smooth with the appearance of being self-sintered. This result is attributed to a high adiabatic flame temperature of decomposition and a high Ag content in the Ag_2BTA complex relative to the other MBTA complexes (which have metal:BTA ratios of less than one).

To overcome this problem, various techniques involving the addition of a so-called gas generate to combustion pellets of Ag_2BTA were investigated. The selection of the gas generate, dihydrazinium bistetrazole, was based on considerations of needing a highly reductive environment (dihydrazinium bistetrazole contains a large weight percent of hydrogen) as well as having a relatively low heat of combustion to reduce the adiabatic flame temperature below the melting point of Ag. Combustion synthesis with these hybrid pellets resulted in a smoke containing disperse Ag nanoparticles rather than a monolithic material, which, while an interesting approach for the production of Ag nanoparticles, was not desired. This result implies that incorporation of a gas generate as implemented is not a suitable technique for decreasing the density of a metallic nanofoam, although a more aggressive mixing method that would enable nanoscale mixing of Ag_2BTA and gas generate could give a mixture that behaves as a single averaged molecule.

However, if instead, pellets of Ag_2BTA and 10–50 wt% dihydrazinium bistetrazole are slowly heated to 500°C in a reducing environment (such as H_2), both decomposition of the Ag_2BTA and simultaneous heat-treatment occurs, yielding an intact Ag nanofoam monolith (Figure 14) with approximately the same aspect ratio of the pressed precursor piece. This in situ reduction process is not unlike that of the work of Erri et al. involving pyrolysis and reduction of $AgNO_3$ on a dextran template, although nanofoams produced with Ag_2BTA exhibit much finer structure.

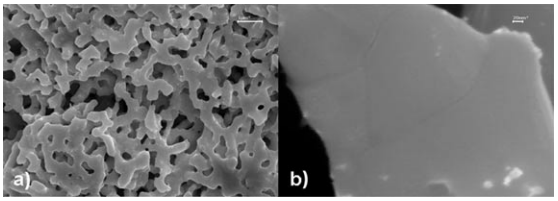

Figure 14. Ag nanofoam formed from the slow decomposition of Ag_2BTA + 10% dihydrazinium bistetrazole gas generate: a) 10000× magnification (scale bar is 1 μm) and b) 200000× magnification (scale bar is 20 nm).

4.4.5. *Inclusion of Metal Nanoparticles*

Inclusion of nanoparticles among with the metal complex in the combustion pellet is another approach for facilitating nanofoam formation in difficult-to-form nanofoams. This approach reduces gas production and provides additional thermal mass that aids in cooling the combustion flame. Proper combustion synthesis of pellets of Ag_2BTA (as opposed to the in situ reduction discussed in Section 4.4.4)

can in fact be achieved by including Ag nanoparticles dispersed throughout the combustion pellet. Combustion synthesis of these mixed pellets results in monoliths with a very fine nanostructure, finer than the in situ reduction approach, but accordingly the shape of the pre-combustion piece is not preserved. It is hypothesized that these nanoparticles uptake excess heat generated from the combustion of Ag_2BTA by undergoing melting, heat that would otherwise sputter Ag released from decomposition of the complex. Slow decomposition by in situ reduction of these pellets also works well. EDAX spectra reveal that, like other nanofoams, as-produced the Ag nanofoams contain small amounts of residual carbon and nitrogen in addition to Ag metal. Complete removal of these carbon- and nitrogen-containing by-products is effectively achieved through heat treatment in an atmosphere of 6% H_2 gas in argon at 500 °C (as determined by thermogravimetric analysis). EDAX of the heat-treated material indicates a composition of essentially pure metallic silver.

We have also demonstrated the ability to incorporate other nanomaterials into a metallic nanofoam matrix through the dispersion of the nanomaterial of interest into pressed MBTA combustion pellets including ceria nanoparticles dispersed in copper nanofoam, carbon nanotubes dispersed in both copper and iron nanofoams, and various combinations of metal nanoparticles in metal nanofoams. Nanocomposites of copper with ceria have shown promise for hydrocarbon conversion catalysts while nanocomposites of copper with carbon nanotubes have demonstrated viability as field emission electrodes.

4.5. Metal Nanofoams of Interest and Their Applications

4.5.1. Titanium-Based Nanofoams for Medical Implants and Solar Energy

Ti nanofoams have been synthesized and show impressive mechanical strength. The successful synthesis of Ti nanofoams demonstrates the flexibility of the MBTA combustion synthesis approach. Most Ti precursors suitable for preparing MBTA complexes are also reactive with water (for example, $TiCl_4$), and so a non-aqueous synthetic route for preparing these complexes had to be established. BTA is insoluble in many aprotic polar organics (such as DMF) useful in solubilizing easily hydrolyzed metal chlorides. Instead, a simple pathway employing Ti alkoxide in ethanol proved to be effective: TiBTA can be produced by the reaction of $Ti[OCH(CH_3)_2]_4$ with two equivalents of BTA in dry alcohol (Scheme 2).

From an applications perspective, titanium is valuable because it has the highest strength-to-weight ratio of any elemental metal, is highly corrosion resistant, and is considered to be physiologically inert. The combination of these properties makes Ti widely useful for applications ranging from aerospace to medical implants. As such, fabrication of titanium nanofoams would have implications in many fields. In the medical arena, titanium is compatible for osseointegration, that is, the direct connection of underlying living bone and structural implant.[117] As a lightweight material, titanium is prized, and combining it with the open, porous structure of a nanofoam invites the possibility of even lighter weight stiff structural materials using Ti nanofoams as foam cores in sandwich panels.[118] Figure 15a shows a SEM image

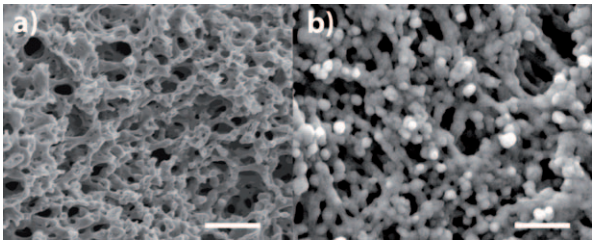

Figure 15. a) SEM image of titanium nanofoam synthesized under inert gas (scale bar is 500 nm) and b) SEM image of titanium dioxide nanofoam synthesized by oxidation of titanium metal nanofoam in air (scale bar is 1 μm).

of Ti nanofoam produced from TiBTA ignited under inert atmosphere. Ti nanofoams exhibit a surface area of 5590 $m^2 mol^{-1}$ (70 $m^2 g^{-1}$), robust monolithicity, and pores in the range of hundreds of nanometers as well as a substantial amount of micron-diameter macroporosity—advantageous for biomedical applications, such as osseointegration, where penetrability by cells is an important consideration.

If pellets of TiBTA are ignited in air instead of inert atmosphere, a coherent titania (TiO_2) nanofoam with macroporosity can be produced (Figure 15b). In contrast with metal foams produced by combustion synthesis, XRD analysis shows titania nanofoams exhibit an essentially amorphous structure with broad peaks corresponding to anatase (not shown). Alternatively and somewhat unexpectedly, Ti nanofoams can be oxidized in air to yield crystalline titania nanofoams which, surprisingly, retain their structural integrity after oxidation. Titania nanofoams produced through this method exhibit a mixture of anatase and rutile titanium dioxide as identified by XRD (Figure 16) and, while probably not as high in surface area as titania aerogels, the macroporosity and crystallinity of titania nanofoams makes them potentially valuable in other respects. Dye-sensitized solar cells (DSSC) are one application that could benefit from crystalline macroporous titania nanofoams.[119] In DSSCs,

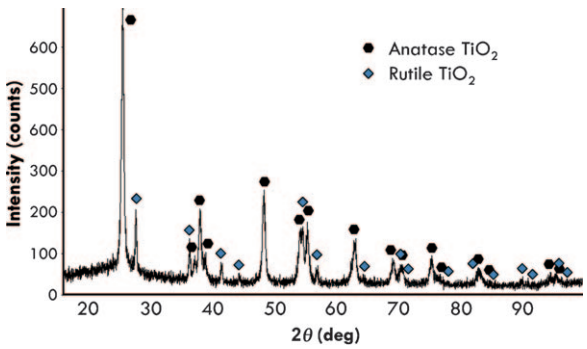

Figure 16. XRD data for a titania nanofoam produced from the oxidation of a titanium metal nanofoam.

photogenerated electrons are created typically by a monolayer of organometallic ruthenium dye deposited on titanium dioxide nanoparticles. The n-type titanium dioxide carries the electron while the holes are passed to an electrolyte. Titania nanofoams provide a coherent nanostructured substrate upon which dye can be deposited and provide facile mass transport for deposition as well as space for multiple layers of film.

Synthesis of MBTA complexes of other metals for which there are no good water-compatible precursors, for example, Zr, Hf, and Si, may also be possible using the alkoxide synthetic approach. Additionally, the capability of Ti nanofoams to retain cohesiveness upon oxidation in air is not unique to Ti and demonstrates how metal nanofoams can serve as precursors to other porous materials, for example, oxides and nitrides.

4.5.2. *Nickel Nanofoams as Low-Cost Catalysts*

Nanostructured nickel is a potentially low-cost alternative to precious-metal catalysts. The requirement for this is an electronic band structure that promotes the reaction of interest and a specific high surface area to maximize reagent contact. An example is the use of so-called "skeletal catalysts", "sponge metal catalysts", or "Raney nickel", that is, high-surface-area nickel structures produced by leaching, or dealloying, of aluminum from NiAl alloy with sodium hydroxide to isolate a porous Ni material. These catalysts have been used for many organic processes including hydrogenation, ammonolysis, reductive alkylations, and dehydrogenation.[68] Importantly, though, a substantial amount (up to 25 wt%) of Al remains even after leaching.[68]

Porous nickel is also used as an electrode in fuel cells, batteries, and hybrid supercapacitors.[120] The higher surface area of porous metals allows the electrolyte to access more of the metal, resulting in faster charge/discharge characteristics. Nickel is typically used as the positive electrode, being one of few materials that can withstand repeated cycling and the associated volumetric changes.[121]

Nickel metal nanofoams have been produced by combustion synthesis of NiBTA. Figure 17 shows an SEM image of a typical Ni nanofoam. As-produced Ni nanofoams exhibit poor monolithicity but achieve a surface area of approximately 2110 $m^2 mol^{-1}$ (36 $m^2 g^{-1}$). This value compares reasonably well with the 1200–5900 $m^2 mol^{-1}$ (20 to 100 $m^2 g^{-1}$) typical for Raney nickel.[68] Figure 18 shows a powder X-ray diffraction (XRD) pattern for a Ni nanofoam. A curious product of the combustion synthesis is the presence of both the typical cubic form of nickel as well as the less-common hexagonal form. The implications of this result on catalytic activity have not yet been evaluated. Furthermore, unlike Raney Ni catalysts which contain residual Al, Ni nanofoams produced from this process contain metallically pure Ni.[122]

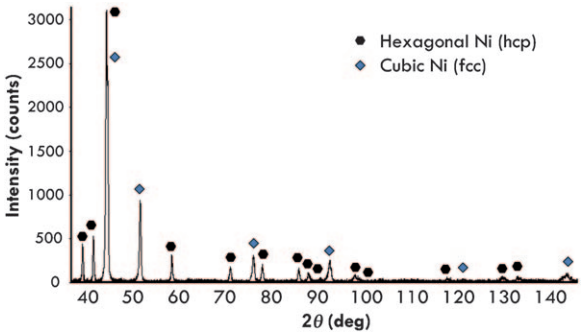

Figure 18. XRD data for nickel nanofoam showing cubic (blue diamonds) and hexagonal (black hexagons) crystal phases of Ni.

4.5.3. *Metal Nanofoam–Nanoparticle Nanocomposites*

As discussed in Section 4.4.5, nanofoams of poorly behaved MBTA complexes can be stabilized by inclusion of nanoparticles of the target metal in the energetic pellet. Nanocomposites of metal nanofoams containing discrete metal nanoparticles of other metals can also be prepared in this way. A metal–metal nanocomposite of interest is produced through the inclusion of nickel nanoparticles into a copper nanofoam matrix (Figure 19a). This material is interesting for catalytic applications as the Ni and Cu remain segregated, thus retaining their separate characteristics in terms of catalysis and electrical/thermal conductivity rather than exhibiting properties of NiCu alloys. This arrangement invites a pathway for producing heterogeneous metal catalysts with high catalytic specificity by leveraging multiple segregated metals in the same catalyst.

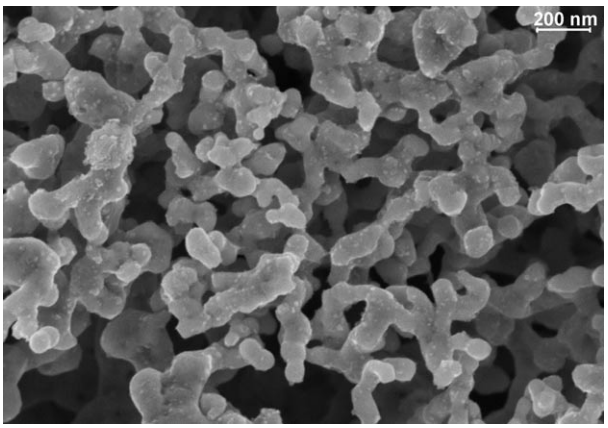

Figure 17. SEM image of Ni nanofoam produced by combustion synthesis, exhibiting a surface area comparable to Raney Ni (scale bar is 200 nm).

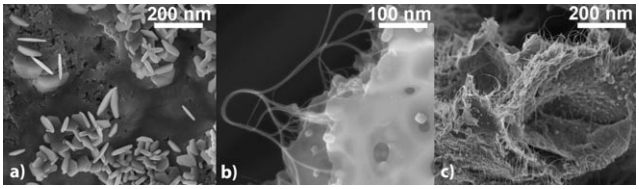

Figure 19. a) Copper nanofoam with embedded hexagonal Ni nanoparticles. b) Copper nanofoam with introduced CNTs. c) Iron nanofoam with introduced CNTs.

Because of interest in the direct oxidation of hydrocarbons for fuel cells and water–gas shift catalysts,[123] we have also prepared composites of Cu nanofoam with 11 nm ceria nanoparticles. Much like the nanoparticulate metals, the ceria nanoparticles were found to retain their composition and structure in the Cu nanofoam matrix, and by back-scatter imaging and EDAX, we determined the particles to be homogenously dispersed.

The inclusion of carbon nanotubes (CNTs) within metal matrixes has attracted attention because of the possibility of dramatically increased strength and thermal and electrical conductivity. Successfully doing so is difficult, however, and most techniques for making metal–CNT composites rely on powder metallurgy procedures, which limit the homogeneity achieved in the composite in addition to limiting the intimacy of contact between the CNTs and metal. Standard melt-processing of such composites is not useful owing to the need for high temperatures that damage the CNTs in addition to high melt viscosities that limit mixing of CNTs. An interesting approach utilizing a combustion synthesis technique has been developed by Groven and Puszynski that allows for inclusion of CNTs within NiAl metallic alloys and TiB_2 ceramics by utilizing the heat associated with the formation of these intermetallics.[124] Their technique shows that even at the high temperatures achieved during the intermetallic reaction the CNTs remain intact, although the composition of composites that can be prepared with this technique is limited to binary systems that undergo intermetallic reactions, and dispersal resolution is limited to the grain size of the precursor powders. Inclusion of CNTs into metallic nanofoams has been demonstrated for the cases of iron and copper, and appears to result in close contact between metal and CNT, as well as a high degree of homogeneity (Figure 19b,c).

4.5.4. *Palladium Nanofoams for Catalysis and Hydrogen Storage*

Palladium is a well-established catalyst in organic synthesis.[125] It is considered to be one of the most versatile catalysts for C–C bond formation and is well-known for its hydrogen permeability. Bulk palladium also reversibly stores a remarkable amount of hydrogen, up to 900 times its volume at room temperature; although in nanosized palladium, desorption is not completely reversible.[126] Although these discoveries date back to the 19th century, invigorated interest in Pd came with the advent of hydrogen fuel cells both in the need to store hydrogen and in the need to filter impurities from the hydrogen feed stream.

We synthesized palladium nanofoams as a model system to study the adsorption–desorption kinetics and reversibility of hydrogen storage with the goal of improving the kinetics of hydrogen storage in commercially viable hydrogen-storage alloys, for example, $LaNi_5$.

PdBTA pellets roughly double in volume upon combustion, affording fragile black Pd nanofoam monoliths. SEM images (Figure 20) shows an extremely fine structure with a polymodal pore size distribution centered in the range of 100–200 nm, with structural elements consisting of particles roughly 10–20 nm in diameter. The finer structural features of the walls are better appreciated under TEM (Figure 20c,d).

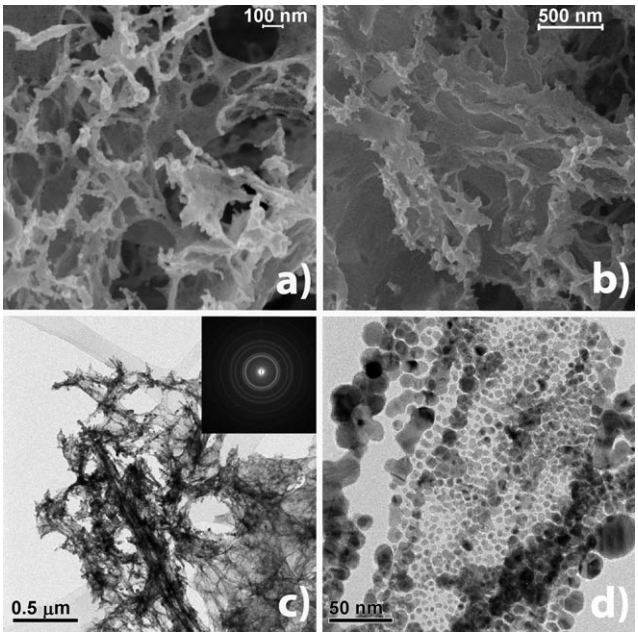

Figure 20. a, b) SEM images of Pd nanofoam formed at 3.5 MPa nitrogen overpressure a) before hydrogen uptake and release and b) after 20 hydrogen-uptake/release cycles; c) TEM image of Pd nanofoam; d) TEM image showing fine grain structure of Pd nanofoam.

The BET surface area of Pd nanofoams formed at 3.5 MPa overpressure was 3900 $m^2 mol^{-1}$ (36.5 $m^2 g^{-1}$).

The hydrogen sorption properties of Pd nanofoams were evaluated by collection of isotherms in static hydrogen at pressures up to 1000 mbar at various temperatures. Identical isotherms were also performed on macrocellular palladium foam, powder (ca. 0.5 μm diameter), and sheet (ca. 0.1 mm thick). Figure 21 shows a representative isotherm at 50 °C for Pd nanofoam compared with Pd powder. As seen in Figure 21, the kinetics of adsorption for both the powder and nanofoam are quite fast; however, there is a significant difference in the curve profiles. The nanofoam was found to uptake hydrogen more rapidly than the powder, although the total uptake volume in the nanofoam was found to be about half that of powder or sheet. A decrease in hydrogen capacity of the nanofoam was somewhat expected because of the lower purity of the Pd produced by the combustion process. Figure 20d shows an SEM image of the nanofoam after 20 hydrogen adsorption/desorption cycles. No obvious physical degradation of the foam has taken place. Overall Pd

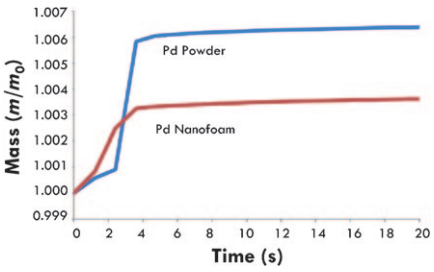

Figure 21. Hydrogen-uptake performance of Pd nanofoam compared to commercially available Pd powder. Pd nanofoams show promise for rapid uptake, outperforming the powder in initial uptake.

nanofoams show great promise for rapid hydrogen storage and can probably be further improved through purification and additional enhancement of surface area.

4.5.5. *Size-Effect-Enhanced Gold Nanofoam Catalysts*

Although gold is usually considered a catalytically inactive metal because of its completely filled 5d orbital and high first ionization energy,[127] nanostructured gold has been shown to be catalytic. Some examples of gold catalysis are the epoxidation of propenes,[128] low-/room-temperature oxidation of CO to CO_2,[5] and recently, growth of single- and multi-walled carbon nanotubes by chemical vapor deposition.[129–131] As a result, nanostructured Au can potentially be used in place of costly bulk Pt, Pd, and Rh used in heterogeneous catalysis.

Gold nanofoams have been produced by combustion synthesis from two different BTA precursors—one surprisingly energetic complex containing three BTA ligands, and one less-energetic complex containing two BTA ligands and one aqua ligand bound to the metal center (as determined by X-ray crystallography). Accordingly the burning rate varies by almost an order of magnitude between these materials (1.3 vs. 16 $cm\,s^{-1}$). Nanofoams produced from the two precursors also contain different concentrations of volatiles. As-produced, the faster-burning complex yields foams containing approximately 95 wt% Au as determined by EDAX. The surface area of these nanofoams was determined by BET analysis to be 2030 $m^2\,mol^{-1}$ (10.9 $m^2\,g^{-1}$) which, as far as we are aware, is the highest surface area reported for a coherent form of Au. The slower-burning complex notably yields nanofoams with bulk density of only 0.057 $g\,cm^{-3}$ or only 0.3% relative density—to our knowledge the lowest density form of coherent gold reported to date. The mechanical properties of these foams are distinct from other metal nanofoams we have prepared in that they are remarkably elastic. Figure 22 shows SEM and TEM images of Au nanofoams produced from these two complexes.

Electrical conductivity of Au nanofoams can be tailored by the controlled annealing of impurities out of the foam. The Au nanofoams were annealed under a flow of 40 sccm ($=cm^3\,min^{-1}$) of a 6% H_2 in Ar mixture at 550°C for 4 h. Two-point probe conductivity measurements of the annealed foams revealed a conductivity of approximately 150 $\Omega\,cm^{-1}$ for the slow-burning foam but only approximately 5 $\Omega\,cm^{-1}$ for the fast-burning foam. Conductivities of the annealed foams were approximately 10^6 times higher than the unannealed precursors, perhaps because of an increase in crystallinity and removal of non-conductive impurities.

To evaluate the catalytic activity of Au nanofoams, chemical vapor deposition (CVD) growth of carbon nanotubes (CNTs) was attempted. It has been previously demonstrated that gold nanoparticles can catalyze CVD growth of CNTs, and so we reasoned that Au nanofoams could potentially do the same as they contain a large area of nanosized surface features which, as a result of size effects, could potentially render the Au catalytically active. CVD processing was performed using a Lindberg/Blue M electric clamshell furnace with a 2.54 cm diameter fused quartz process tube. Volatile organic impurities of Au nanofoams from the fast-burning complex were removed by heating from room temperature to 750°C under a flow of 73 sccm He over the course of 20 min, followed by cooling to room temperature under 925 sccm of He. The annealed foams were then processed by CVD by ramping to 750°C over the course of 20 min under a flow of 73 sccm He and 400 sccm H_2, then adding a flow of 121 sccm C_2H_4, waiting 30 min, and finally cooling to ambient conditions under a flow of 925 sccm of He. SEM images (Figure 23) revealed larger (ca. 1.5 micron) struts after annealing compared with unannealed foams. After CVD, macroscopically visible black tufts ca. 0.5 mm high could be seen on the otherwise yellow–orange Au nanofoam monolith. SEM images of the foams revealed high-yield growth of carbon nanofiber (CNFs) and carbon nanotube tufts. Bundles of defective, multi-walled CNTs were

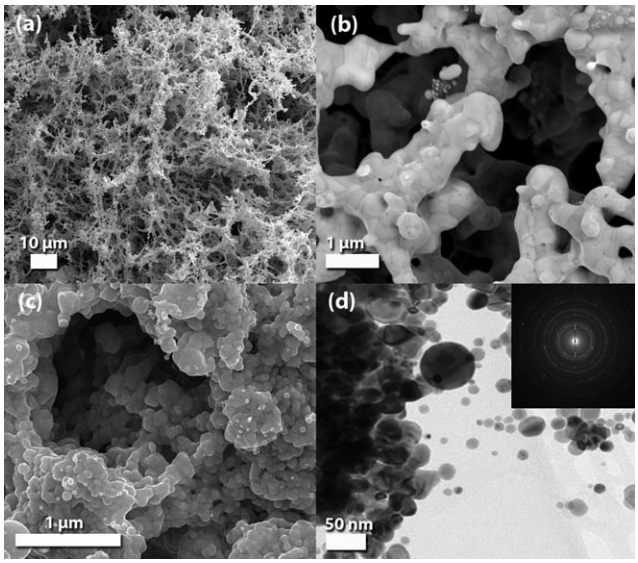

Figure 22. SEM images of Au foams produced a) from $[Au(BTA)_2(NH_4)(H_2O)]\cdot 2H_2O$ and b, c) from $[Au(BTA)_3(NH_4)_3]$, both combusted under 6.89 MPa Ar overpressure; d) TEM image with electron diffraction pattern of Au nanofoam derived from $[Au(BTA)_3(NH_4)_3]$ revealing a fine nanostructure.

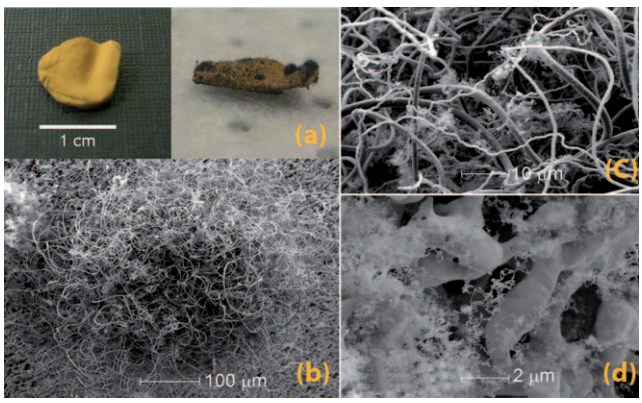

Figure 23. Demonstration of catalytic growth of CNTs and CNFs on Au nanofoam produced from fast-burning $AuBTA_3$ complex. a) Macroscopic view before (left) and after (right) CNT growth; b) SEM image of large tuft of CNTs and CNFs; c) higher magnification of CNTs/CNFs in a tuft; d) CNTs extending directly from struts of the nanofoam.

found hugging the globular struts of the nanofoams at all locations on the monolith. To our knowledge, this represents the first demonstration of high-yield growth of fibrous carbon nanostructures directly upon a monolithic gold substrate. Additionally, since the conductivity of Au nanofoams can be tailored through controlled annealing, this provides a mechanism for the growth of CNTs on a conductive substrate with tailorable electrical conductivity.

4.5.6. *Solid-State Conversion of Carbon into CNTs and CNFs*

Interestingly, we have found that is also possible to transform the organic impurities leftover from combustion synthesis into carbon nanotubes (CNTs) and carbon nanofibers (CNFs) through a solid-state process.

Upon exposure of as-produced Co nanofoams to a 63 W continuous-wave 10.6 μm CO_2 laser in inert atmosphere, CNTs and CNFs were observed on the nanofoam surface (Figure 24, top). As the only source of carbon present to contribute to production of CNTs/CNFs in this process was carbon from organic impurities in the nanofoam, it appears that a solid-state transformation of the residual carbon-containing compounds into carbon nanostructures occurs. Notably, CNTs/CNFs over 10 μm in length result from only 1 s of exposure. Portions of Co nanofoams containing CNT/CNF growth were easily separated from those exhibiting no growth by using a magnet: only regions of the foam exposed to the laser result in growth of CNTs and CNFs and the Co in these regions is rendered magnetic when the impurities are removed (transformed into CNTs) while regions not contacted by the laser remain non-magnetic.

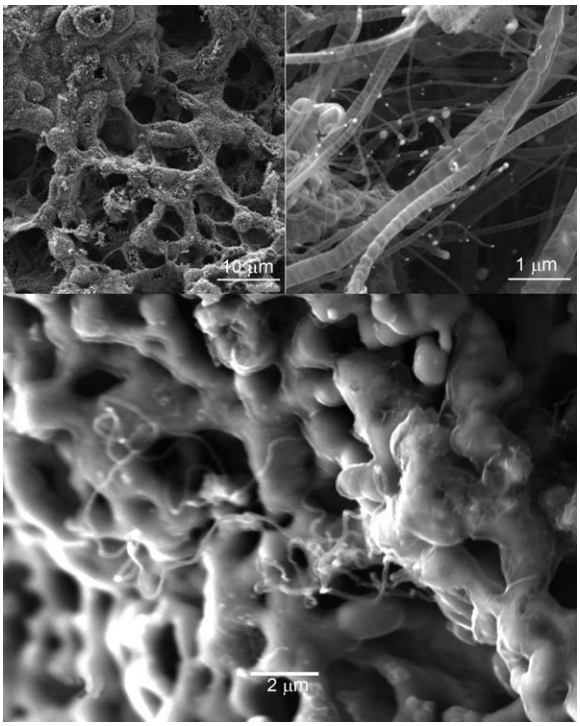

Figure 24. Top: Solid-state laser-flash growth of CNTs and CNFs from carbon impurities on Co foams by 10.6 μm laser irradiation. Bottom: smaller diameter CNTs grown by CVD on annealed Co nanofoam.

We see this technique as a novel pathway for growing CNTs on electrically conductive substrates, which is frequently difficult to achieve because of the reactivity of carbon with metals at the typical temperatures used for CVD growth of CNTs (usually > 600 °C). Since this approach involves only localized heating, it is interesting to consider if it could be adapted for use in CMOS-compatible (CMOS = complementary metal oxide semiconductors) production of CNT-based vias or transistors (since CVD growth of CNTs typically occurs well above the melting point of several materials used in CMOS processing thus precluding CVD processing of entire CMOS substrates, especially for back-end processing).

Annealed Co nanofoams are also effective catalysts for CVD growth of CNTs and result in smaller diameter CNTs than the solid-state laser-flash approach, but in much lower yield. In a typical experiment, a Co nanofoam is annealed under a flow of 200 sccm H_2 at 500 °C for 30 min, after which it is ramped to 700 °C under a flow of 400 sccm H_2 and 100 sccm He. Once at temperature, a flow of 100 sccm C_2H_4 is added to initiate CNT growth. After 10 min the C_2H_4 and H_2 are removed and the nanofoam is cooled to ambient conditions. CNTs can be found hugging the surface of the nanofoam after CVD processing (Figure 24, bottom), indicating the presence of nanosized Co particles throughout the nanofoam that can serve as seeds for the CNT growth process. Indeed, the presence of Co nanoparticles is observed by TEM.

4.5.7. *Other Applications*

Further promising applications of metal nanofoams that we have investigated include surface-enhanced Raman spectroscopy, cold field emission substrates, high-field magnets, and production of fuel cell anodes using Cu/CeO_2 nanofoam for direct oxidation of hydrocarbons. Measurements of the propensity of metal nanofoams towards catalyzing various chemical reactions of industrial importance are also underway.

5. Summary and Outlook

With the advent of aerogels in the 1930s the field of high-surface-area nanoporous foams was born, and over the past two decades this field has been extended to a wide variety of new substances and morphologies. Finally the frontier of nanoporous foams includes metals and alloys. Numerous potential breakthroughs await in the nascent field of NMFs thanks to the disparate materials properties and chemical properties they combine.

In this Review, we have presented an overview of the state of the art in production of nanoporous metal foams as well potential applications of them. Now that synthetic pathways for preparing NMFs have been demonstrated, their applications in the development of technologies including new nanostructured catalysts, 3D electrochemical energy-storage architectures, viable hydrogen-storage materials, electromagnetic composites, and lightweight structural materials can be explored. The most promising techniques for producing NMFs demonstrated thus far appear to be the nanosmelting

technique of Leventis and combustion synthesis employing MBTA complexes. These two approaches offer production of true nanoporous materials, the possibility to extend the approach to most metals, and potential for scalability. With further refinement, numerous other techniques may also become viable. Lessons learned in the development of these two platforms may also aid in inspiring new synthetic pathways for the production of NMFs.

Significant work remains be done to characterize the catalytic propensity and electrochemical activity of NMFs and to understand how these nanoarchitectures are like and unlike nanoparticulate and bulk metals. Development of methods for controlling porosity over nano, micro, and macro length scales and strategies for controlling monolithicity will be important for maximizing the potential of NMFs for technological applications. Characterization of the mechanical behavior of NMFs will be important for assessing the potential of using NMFs in ultralightweight structures and impact dissipation media. Characterization of thermal and electrical transport will be important for energy-storage applications.

Combustion synthesis of MBTA complexes has proven to be a flexible, general approach for the formation of a wide range of nanoporous metal foams of a large number of metals of varying chemistries. Unlike many other techniques used in the preparation of porous metals, combustion synthesis combined with simple post-combustion heat treatments enables the production of metallically pure NMFs. Additionally, nanofoams produced by combustion synthesis can be derivatized without losing structural integrity. Post-processing techniques can be performed to improve strength, increase surface area, and promote phase changes, capabilities that are valuable for production of nanoporous alloys where control over grain size and crystallographic phase are important. While the general approach for preparing NMFs of essentially any transition- or main-group-metal through combustion synthesis of MBTA complexes has already been outlined, many MBTA complexes have yet to be synthesized and characterized. Understanding the energetic behavior of these complexes will be important for achieving the full potential of the approach, for example, to produce nanofoams of alloys, such as stainless steel and amorphous metal. More advanced BTA complexes containing bridging metal atoms, multiple different metal atoms, and combinations of non-energetic and energetic ligands, for example, may enable additional compositions and morphologies of NMFs not yet achieved. Furthermore, it is reasonable to speculate that there are other energetic ligands that exhibit a "Goldilocks effect" similar to BTA which could be used to facilitate additional degrees of freedom in nanofoam combustion synthesis.

This said, no viable pathways for preparing NMFs of alkali- or alkaline-earth-metals currently exist. Synthetic strategies for preparing NMFs of Li, for example, would be valuable for the battery industry. Likewise, Mg NMFs would be valuable for production of lightweight alloys, efficient Grignard reagents, and explosives. Development of new pathways for preparing NMFs will be required to access these compositions.

Innovation and accident seem to go hand-in-hand in this age of nano as we strive to understand nature's length-scale peculiarities. And as brute-force approaches fail us (and we continue hammering away at them despite), elegant and unsuspecting pathways can pop up somewhere else, staring us straight in the eye while we label them as process bugs and unintended results. We take the unintended discovery of combustion synthesis of metal nanofoams as a preparatory lesson that breakthrough technologies lay all around us if we are willing to remain vigilant and open-minded in our interpretation of nature's responses to our queries—a useful reminder as we plow forth to reveal the potential of this exciting new frontier of materials.

We gratefully acknowledge the support of the U.S. Department of Energy through the LANL/LDRD Program for this work. The Los Alamos National Laboratory is operated by Los Alamos National Security for the U.S. Department of Energy's National Nuclear Security Agency. We thank Dr. Daniel Pressl for his diligent translation of this Review into German, Prof. Nicholas Leventis and Dr. Juergen Biener for scientific contributions, Dr. Joseph Mang for USANS measurements and analysis, Dr. Brian Scott for determination of the X-ray crystal structure of CoBTA, Dr. Oktay Uzun for donation of nanoparticles, and Prof. Petey Young, Prof. Robert West, Dr. Jackie Veauthier, Dr. Gregory Long, Dr. Desirée Plata, Prof. A. John Hart, Dr. John Mills, and Dr. Lauren DeFlores for helpful conversations and edits.

Received: June 3, 2009
Revised: September 10, 2009
Published online: May 31, 2010

[1] I. Zuburtikudis, H. Saltsburg, *Science* **1992**, *258*, 1337.
[2] M. Haruta, T. Kobayashi, H. Sano, N. Yamada, *Chem. Lett.* **1987**, 405.
[3] M. Haruta, K. Saika, T. Kobayashi, S. Tsubota, Y. Nakahara, *Chem. Express* **1988**, *3*, 159.
[4] D. Cunningham, S. Tsubota, N. Kamijo, M. Haruta, *Res. Chem. Intermed.* **1993**, *19*, 1.
[5] *Nanoparticles and Catalysis* (Ed.: D. Astruc), Wiley-VCH, Weinheim, **2008**.
[6] M. C. Dixon, T. A. Daniel, M. Hieda, D. M. Smilgies, M. H. W. Chan, D. L. Allara, *Langmuir* **2007**, *23*, 2414.
[7] T. M. Tillotson, L. W. Hrubesh, *J. Non-Cryst. Solids* **1992**, *145*, 44.
[8] K. A. DeFriend, B. Espinoza, B. Patterson, *Fusion Sci. Technol.* **2007**, *51*, 693.
[9] S. S. Kistler, *Nature* **1931**, *127*, 741.
[10] S. S. Kistler, *J. Phys. Chem.* **1932**, *36*, 52.
[11] A. E. Gash, T. M. Tillotson, J. H. Satcher, Jr., L. W. Hrubesh, R. L. Simpson, *J. Non-Cryst. Solids* **2001**, *285*, 22.
[12] J. F. Poco, J. H. Satcher, Jr., L. W. Hrubesh, *J. Non-Cryst. Solids* **2001**, *285*, 57.
[13] W. Dong, B. Dunn, *J. Non-Cryst. Solids* **1998**, *225*, 135.
[14] F. Chaput, B. Dunn, P. Fuqua, K. Salloux, *J. Non-Cryst. Solids* **1995**, *188*, 11.
[15] R. A. Reibold, J. F. Poco, T. F. Baumann, R. L. Simpson, J. H. Satcher, Jr., *J. Non-Cryst. Solids* **2003**, *319*, 241.
[16] J. H. Harreld, J. Sakamoto, B. Dunn, *J. Power Sources* **2003**, *115*, 19.

[17] Q. Yao, I. U. Arachchige, S. L. Brock, *J. Am. Chem. Soc.* **2009**, *131*, 2800.
[18] S. L. Brock, I. U. Arachchige, J. L. Mohanan, *Science* **2005**, *307*, 397.
[19] K. Senevirathne, R. Tackett, P. R. Kharel, G. Lawes, A. Burns, M. E. Bussell, S. L. Brock in *Abstracts of the Central Regional Meeting of the American Chemical Society*, Cleveland, **2009**.
[20] R. W. Pekala, C. T. Alviso, J. D. LeMay, *J. Non-Cryst. Solids* **1990**, *125*, 67.
[21] R. Brandt, R. Petricevic, H. Pröbstle, J. Fricke, *J. Porous Mater.* **2003**, *10*, 171.
[22] R. W. Pekala, C. T. Alviso, F. M. Kong, S. S. Hulsey, *J. Non-Cryst. Solids* **1992**, *145*, 90.
[23] M. A. Worsley, S. O. Kucheyev, J. D. Kuntz, A. V. Hamza, J. H. Satcher, Jr., T. F. Baumann, *J. Mater. Chem.* **2009**, *19*, 3370.
[24] M. B. Bryning, D. E. Milkie, M. F. Islam, L. A. Hough, J. M. Kikkawa, A. G. Yodh, *Adv. Mater.* **2007**, *19*, 661.
[25] M. F. Ashby, A. G. Evans, N. A. Fleck, L. J. Gibson, J. W. Hutchinson, H. N. G. Wadley, *Metal Foams: A Design Guide*, Butterworths Heinemann, Oxford, **2000**.
[26] L. J. Gibson, *Annu. Rev. Mater. Sci.* **2000**, *30*, 191.
[27] C.-J. Yu, H. Eifert, *Adv. Mater. Processes* **1998**, November, 45.
[28] J. Baumeister, USPTO patent 5,151,246, **1988**.
[29] ERG Aerospace Corporation, DUOCEL Aluminum Foam, http://www.ergaerospace.com/foamproperties/literature/erg_duocel.pdf, **2009**.
[30] J. Babjak, V. A. Ettel, V. Paserin, USPTO patent 4,957,543, **1990**.
[31] Y. Sharpalov, *MRS Bull.* **1994**, *April*, 24.
[32] A. E. Simone, Jr., PhD thesis, Massachusetts Institute of Technology (Cambridge, MA), **1997**.
[33] J. Erlebacher, *J. Electrochem. Soc.* **2004**, *151*, C614.
[34] Y. Ding, J. Erlebacher, *J. Am. Chem. Soc.* **2003**, *125*, 7772.
[35] J. Erlebacher, M. J. Aziz, A. Karma, N. Dimitrov, K. Sleradzki, *Nature* **2001**, *410*, 450.
[36] K. Shin, K. A. Leach, J. T. Goldbach, D. H. Kim, J. Y. Jho, M. Tuominen, C. J. Hawker, T. P. Russell, *Nano Lett.* **2002**, *2*, 933.
[37] C. L. Liao, C. W. Chu, K. Z. Fung, I. C. Leu, *J. Alloys Compd.* **2007**, *441*, L1.
[38] O. Näth, A. Stephen, J. Rösler, F. Vollertsen, *J. Mater. Process. Technol.* **2009**, *209*, 4739.
[39] G. W. Nyce, J. R. Hayes, A. V. Hamza, J. H. Satcher, Jr., *Chem. Mater.* **2007**, *19*, 344.
[40] N. Leventis, N. Chandrasekaran, A. G. Sadekar, C. Sotiriou-Leventis, H. Lu, *J. Am. Chem. Soc.* **2009**, *131*, 4576.
[41] N. Chandrasekaran, N. Leventis, C.-S. Leventis, A. Mumtaz, Abstracts of Papers, 237th ACS National Meeting, Salt Lake City, USA, March 22–26, **2009**, COLL.
[42] B. C. Tappan, M. H. Huynh, M. A. Hiskey, D. E. Chavez, E. P. Luther, J. T. Mang, S. F. Son, *J. Am. Chem. Soc.* **2006**, *128*, 6589.
[43] X. Lu, O. Nilsson, J. Fricke, R. W. Pekala, *J. Appl. Phys.* **1993**, *73*, 581.
[44] J. Wang, S. Q. Zhang, Y. Z. Guo, J. Shen, S. M. Attia, B. Zhou, G. Z. Zheng, Y. S. Gui, *J. Electrochem. Soc.* **2001**, *148*, D75.
[45] D. R. Rolison, J. W. Long, J. C. Lytle, A. E. Fischer, C. P. Rhodes, T. M. McEvoy, M. E. Bourg, A. M. Lubers, *Chem. Soc. Rev.* **2009**, *38*, 226.
[46] B. Dunn, J. W. Long, D. R. Rolison, *Electrochem. Soc. Interface* **2008**, *Fall*, 49.
[47] B. Kang, G. Ceder, *Nature* **2009**, *458*, 190.
[48] V. Bérubé, G. Radtke, M. Dresselhaus, G. Chen, *Int. J. Energy Res.* **2007**, *31*, 637.
[49] B. Sakintuna, F. Lamari-Darkrim, M. Hirscher, *Int. J. Hydrogen Energy* **2007**, *32*, 1121.
[50] E. J. Wollack, D. J. Fixsen, R. Henry, A. Kogut, M. Limon, P. Mirel, *Int. J. Infrared Millimeter Waves* **2008**, *29*, 51.
[51] A. I. Maaroof, A. Gentle, G. B. Smith, M. B. Cortie, *J. Phys. D* **2007**, *40*, 5675.
[52] J. Biener, G. W. Nyce, A. M. Hodge, M. M. Biener, A. V. Hamza, S. A. Maier, *Adv. Mater.* **2008**, *20*, 1211.
[53] J. C. Farmer, D. V. Fix, G. V. Mack, R. W. Pekala, J. F. Poco, *J. Electrochem. Soc.* **1996**, *143*, 159.
[54] M. Nishizawa, V. P. Menon, C. R. Martin, *Science* **1995**, *268*, 700.
[55] A. P. Padilla, J. A. Rodriguez, H. A. Saitua, *Desalination* **1997**, *114*, 203.
[56] P. A. Busch, S. P. Cheston, D. S. Greywall, *Cryogenics* **1984**, *24*, 445.
[57] K. A. DeFriend, D. A. Loy, USPTO patent application no. 20060216219, **2006**.
[58] A. J. Hunt, M. R. Ayers, W. Cao, *J. Non-Cryst. Solids* **1995**, *185*, 227.
[59] J. S. King, A. Wittstock, J. Biener, S. O. Kucheyev, Y. M. Wang, T. F. Baumann, S. K. Giri, A. V. Hamza, M. Baeumer, S. F. Bent, *Nano Lett.* **2008**, *8*, 2405.
[60] J. T. Mang, R. P. Hjelm, S. F. Son, P. D. Peterson, B. S. Jorgensen, *J. Mater. Res.* **2007**, *22*, 1907.
[61] S. Brunauer, P. H. Emmett, E. Teller, *J. Am. Chem. Soc.* **1938**, *60*, 309.
[62] E. P. Barrett, L. G. Joyner, P. P. Halenda, *J. Am. Chem. Soc.* **1951**, *73*, 373.
[63] P. Jiang, J. Cizeron, J. F. Bertone, V. L. Colvin, *J. Am. Chem. Soc.* **1999**, *121*, 7957.
[64] H. Yan, C. F. Blanford, B. T. Holland, M. Parent, W. H. Smyrl, A. Stein, *Adv. Mater.* **1999**, *11*, 1003.
[65] Y. Ding, M. Chen, J. Erlebacher, *J. Am. Chem. Soc.* **2004**, *126*, 6876.
[66] M. Raney, USPTO patent no. 1,628,190, **1927**.
[67] R. J. Kokes, P. H. Emmett, *J. Am. Chem. Soc.* **1959**, *81*, 5032.
[68] J. Freel, W. Pieters, R. Anderson, *J. Catal.* **1969**, *14*, 247.
[69] A. Wittstock, B. Neumann, A. Schaefer, K. Dumbuya, C. Kuebel, M. M. Biener, V. Zielasek, H.-P. Steinrueck, J. M. Gottfried, J. Biener, A. Hamza, M. Baeumer, *J. Phys. Chem. C* **2009**, *113*, 5593.
[70] V. Zielasek, B. Jürgens, C. Schulz, J. Biener, M. M. Biener, A. V. Hamza, M. Bäumer, *Angew. Chem.* **2006**, *118*, 8421; *Angew. Chem. Int. Ed.* **2006**, *45*, 8241.
[71] See Ref. [52].
[72] I. U. Arachchige, S. L. Brock, *J. Am. Chem. Soc.* **2006**, *128*, 7964.
[73] S. L. Brock, K. Senevirathne, *J. Solid State Chem.* **2008**, *181*, 1552.
[74] J.-P. Boilot, P. Larregaray, K. Lahlil, T. Gacoin, *J. Phys. Chem. B* **2001**, *105*, 10228.
[75] C. J. Brinker, G. W. Scherrer, *Sol-Gel Science: The Physics and Chemistry of Sol-Gel Processing*, Academic Press, New York, **1990**.
[76] O. Uzun, Y. Hu, A. Verma, S. Chen, A. Centrone, F. Stellacci, *Chem. Commun.* **2008**, 196.
[77] N. Leventis, N. Chandrasekaran, C. Sotiriou-Leventis, A. Mumtaz, *J. Mater. Chem.* **2009**, *19*, 63.
[78] S. Mulik, C. Sotiriou-Leventis, N. Leventis, *Chem. Mater.* **2007**, *19*, 6138.
[79] N. Leventis, personal communication.
[80] See Ref. [40].
[81] F. K. McTaggart, *Nature* **1961**, *191*, 1192.
[82] M. D. Sacks, C.-A. Wang, Z. Yang, A. Jain, *J. Mater. Sci.* **2004**, *39*, 6057.
[83] A. Maitre, P. Lefort, *Actual. Chim.* **1999**, *5*, 35.
[84] J. N. Armor, E. J. Carlson, G. Carrasquillo, *Mater. Lett.* **1986**, *4*, 373.
[85] D. Walsh, L. Arcelli, T. Ikoma, J. Tanaka, S. Mann, *Nat. Mater.* **2003**, *2*, 386.

[86] A. Varma, A. S. Rogachev, A. S. Mukasyan, S. Hwang, *Adv. Chem. Eng.* **1998**, *24*, 79.
[87] P. Erri, J. Nader, A. Varma, *Adv. Mater.* **2008**, *20*, 1243.
[88] E. M. Hunt, M. L. Pantoya, R. J. Jouet, *Intermetallics* **2006**, *14*, 620.
[89] D. E. Chavez, M. A. Hiskey, D. L. Naud, *J. Pyrotech.* **1999**, 17.
[90] M. Friedrich, J. C. Galvez-Ruiz, T. M. Klapötke, P. Mayer, B. Weber, J. J. Weigand, *Inorg. Chem.* **2005**, *44*, 8044.
[91] G. Geisberger, T. M. Klapötke, J. Stierstorfer, *Eur. J. Inorg. Chem.* **2007**, 4743.
[92] A. Hammerl, G. Holl, T. M. Klapötke, P. Mayer, H. Nöth, H. Piotrowski, M. Warchhold, *Eur. J. Inorg. Chem.* **2002**, 834.
[93] K. Karaghiosoff, T. M. Klapötke, C. M. Sabate, *Chem. Eur. J.* **2009**, *15*, 1164.
[94] T. M. Klapötke, P. Mayer, J. Stierstorfer, J. J. Weigand, *J. Mater. Chem.* **2008**, *18*, 5248.
[95] T. M. Klapötke, C. M. Sabate, *New J. Chem.* **2009**, *33*, 1605.
[96] T. M. Klapötke, C. M. Sabate, *Chem. Mater.* **2008**, *20*, 1750.
[97] T. M. Klapötke, C. M. Sabate, *Z. Anorg. Allg. Chem.* **2007**, *633*, 2671.
[98] T. M. Klapötke, C. M. Sabate, *New Trends Res. Energ. Mater., Proc. Semin., 10th*, **2007**, 230.
[99] T. M. Klapötke, C. M. Sabate, *Chem. Mater.* **2008**, *20*, 3629.
[100] T. M. Klapötke, C. M. Sabate, *Dalton Trans.* **2009**, 1835.
[101] T. M. Klapötke, C. M. Sabate, J. M. Welch, *Dalton Trans.* **2008**, 6372.
[102] T. M. Klapötke, J. Stierstorfer, *Helv. Chim. Acta* **2007**, *90*, 2132.
[103] T. M. Klapötke, J. Stierstorfer, B. Weber, *Inorg. Chim. Acta* **2009**, *362*, 2311.
[104] J. Stierstorfer, K. R. Tarantik, T. M. Klapötke, *Chem. Eur. J.* **2009**, *15*, 5775.
[105] L. R. Bates, *Proc. Symp. Explos. Pyrotech., 13th Symp.*, **1986**, III1.
[106] P. M. Dickson, J. E. Field, *Proc. R. Soc. London Ser. A* **1993**, *441*, 359.
[107] J. Sawkill, *Proc. R. Soc. London Ser. A* **1955**, *229*, 135.
[108] See Ref. [60].
[109] Adiabatic flame temperatures were calculated by inputing physical data from Table 2 into the thermoequilibrium code Cheetah V4.0; L. E. Fried, K. R. Glaesemann, W. R. Howard, P. C. Souers, P. A. Vitello, *Cheetah V4.0 User's Manual*, UCRL-CODE-155944, 4.0; Lawrence Livermore National Laboratory: **2004**.
[110] Calculations for Pd and Pt were not available in the product libraries for the thermoequilibrium software used to compute the data and so the adiabatic flame temperature for the combustion of these two complexes could not be determined; however, based on the measured heats of formation for these complexes, their similar molecular weights, and similar chemical formulas, their adiabatic flame temperatures are expected to be well below the melting point of these metals.
[111] A. C. Frank, F. Stowasser, H. Sussek, H. Pritzkow, C. R. Miskys, O. Ambacher, M. Giersig, R. A. Fischer, *J. Am. Chem. Soc.* **1998**, *120*, 3512.
[112] D. L. Naud, M. A. Hiskey, USPTO patent 6,570,022, **2003**.
[113] N. Liu, Q. Yue, Y.-Q. Wang, A.-L. Cheng, E.-Q. Gao, *Dalton Trans.* **2008**, 34, 4621.
[114] T. M. Klapötke, P. Mayer, K. Polborn, J. Stierstorfer, J. J. Weigand in *37th International Annual Conference of ICT (Energetic Materials)*, **2006**, p. 134/1.
[115] Z. A. Munir, *Mater. Sci. Eng. A* **2000**, *287*, 125.
[116] See Ref. [42].
[117] H. Li, S. Oppenheimer, S. Stupp, D. Dunand, L. Brinson, *Mater. Trans.* **2004**, *45*, 1124.
[118] F. Zok, S. Waltner, Z. Wei, H. Rathbun, R. McMeeking, A. Evans, *Int. J. Solids Struct.* **2004**, *41*, 6249.
[119] L. Schmidt-Mende, U. Bach, R. Humphry-Baker, T. Horiuchi, H. Miura, S. Ito, S. Uchida, M. Grätzel, *Adv. Mater.* **2005**, *17*, 813.
[120] M. Bursell, A. Lundblad, P. Bjoernbom, *Proc. Electrochem. Soc.* **2002**, *7*, 116.
[121] S. F. Corbin, R. M. C. Clemmer, Q. Yang, *J. Am. Ceram. Soc.* **2009**, *92*, 331.
[122] As formed, Ni nanofoams contain carbon- and nitrogen-containing impurties, but these are easily removed by heat treatment or chemical etching.
[123] H. Kusar, S. Hocevar, J. Levec, *Appl. Catal. B* **2006**, 63, 194.
[124] L. J. Groven, J. A. Puszynski, *Int. J. Self-Propag. High-Temp. Synth.* **2007**, *16*, 189.
[125] *Palladium in Organic Synthesis* (Ed.: J. Tsuji), Springer, Berlin, **2005**.
[126] H. Kobayashi, M. Yamauchi, H. Kitagawa, Y. Kubota, K. Kato, M. Takata, *J. Am. Chem. Soc.* **2008**, *130*, 1828.
[127] G. Schmid, *Chem. Rev.* **1992**, *92*, 1709.
[128] T. Hayashi, K. Tanaka, M. Haruta, *J. Catal.* **1998**, *178*, 566.
[129] S. Bhaviripudi, E. Mile, S. A. Steiner III, A. T. Zare, M. S. Dresselhaus, A. M. Belcher, J. Kong, *J. Am. Chem. Soc.* **2007**, *129*, 1516.
[130] S. Y. Lee, M. Yamada, M. Miyake, *Carbon* **2005**, *43*, 2654.
[131] M. Yamada, M.-A. Kawana, M. Miyake, *Appl. Catal. A* **2006**, 302, 201.